

Highlights

Adaptive Sampling with PIXL on the Mars *Perseverance* Rover

Peter R. Lawson, Tanya V. Kizovski, Michael M. Tice, Benton C. Clark III, Scott J. VanBommel, David R. Thompson, Lawrence A. Wade, Robert W. Denise, Christopher M. Heirwegh, W. Timothy Elam, Mariek E. Schmidt, Yang Liu, Abigail C. Allwood, Martin S. Gilbert, Benjamin J. Bornstein

- First autonomous decision-making is demonstrated based on real-time compositional analysis.
- Adaptive sampling rules are created using X-ray spectra of rocks observed by the Mars *Perseverance* rover.
- Rules are formulated through machine learning and the analysis of ternary compositional diagrams.
- Ground-based simulations exactly reproduce the behavior observed on Mars.
- Long dwells are reliably triggered for carbonates, phosphate minerals, and spinels.

Adaptive Sampling with PIXL on the Mars *Perseverance* Rover

Peter R. Lawson^{a,*}, Tanya V. Kizovski^b, Michael M. Tice^c, Benton C. Clark III^d, Scott J. VanBommel^e, David R. Thompson^f, Lawrence A. Wade^f, Robert W. Denise^a, Christopher M. Heirwegh^f, W. Timothy Elam^g, Mariek E. Schmidt^b, Yang Liu^f, Abigail C. Allwood^f, Martin S. Gilbert^f and Benjamin J. Bornstein^f

^aRetired - Jet Propulsion Laboratory, California Institute of Technology, 4800 Oak Grove Drive, Pasadena, 91109, CA, USA

^bBrock University, 1812 Sir Isaac Brock Way, St. Catharines, L2S 3A1, ON, Canada

^cTexas A&M University, 3115 TAMU, College Station, 77843-3115, TX, USA

^dSpace Science Institute, 4765 Walnut St, Suite B, Boulder, 80301, CO, USA

^eWashington University in St. Louis, 1 Brookings Drive, St. Louis, 63130, MO, USA

^fJet Propulsion Laboratory, California Institute of Technology, 4800 Oak Grove Drive, Pasadena, 91109, CA, USA

^gUniversity of Washington, 1013 NE 40th St., Seattle, 98105, WA, USA

ARTICLE INFO

Keywords:

Data reduction techniques
Instrumentation
Mars, surface
Spectroscopy

ABSTRACT


Planetary rovers can use onboard data analysis to adapt their measurement plan on the fly, improving the science value of data collected between commands from Earth. This paper describes the implementation of an adaptive sampling algorithm used by PIXL, the X-ray fluorescence spectrometer of the Mars 2020 *Perseverance* rover. PIXL is deployed using the rover arm to measure X-ray spectra of rocks with a scan density of several thousand points over an area of typically 5 x 7 mm. The adaptive sampling algorithm is programmed to recognize points of interest and to increase the signal-to-noise ratio at those locations by performing longer integrations. Two approaches are used to formulate the sampling rules based on past quantification data: 1) Expressions that isolate particular regions within a ternary compositional diagram, and 2) Machine learning rules that threshold for a high weight percent of particular compounds. The design of the rulesets are outlined and the performance of the algorithm is quantified using measurements from the surface of Mars. To our knowledge, PIXL's adaptive sampling represents the first autonomous decision-making based on real-time compositional analysis by a spacecraft on the surface of another planet.

1. Introduction

As successive generations of Mars rovers have become more capable, and their operational objectives more ambitious, they have made increasing use of spacecraft autonomy to achieve their science objectives. Operators have limited communications opportunities with the remote spacecraft, so autonomy can help maximize the productivity of rover activity during the finite mission lifetime (Candela et al., 2017; Wettergreen et al., 2014; Thompson et al., 2011). The Mars 2020 *Perseverance* rover exemplifies this trend. This rover must travel long distances across many geologic units to obtain a diverse collection of samples for return to Earth, traveling quickly between sample sites. Its rapid exploration is made possible by improvements in autonomous navigation (Farley et al., 2020; Verma et al., 2023). Upon reaching a site of interest, the rover has only limited resources for data collection to establish the geologic context. Here autonomy can also play a role, by adapting the data collection activities on the fly and improving the science yield of each command cycle.

This *science autonomy* has been deployed to Mars several times before *Perseverance*. The Mars Exploration Rovers used onboard image analysis to capture images of dust devils on the Mars surface (Castano et al., 2008). The Opportunity rover used onboard rock detection to identify targets of interest for followup imagery during long drives (Estlin et al., 2012). This capability was later developed into an onboard targeting procedure used by the Curiosity rover to point its ChemCam instrument (Francis et al., 2017). All of these algorithms followed a similar pattern in which the rover identified opportunistic science targets in image data and then prioritized key features for followup data collection. Another notable example of science autonomy is the range-finding algorithm used by Curiosity's Alpha Particle X-ray

*Corresponding author.

 prlawson37@gmail.com (P.R. Lawson)

ORCID(s): 0009-0004-6928-1565 (P.R. Lawson)

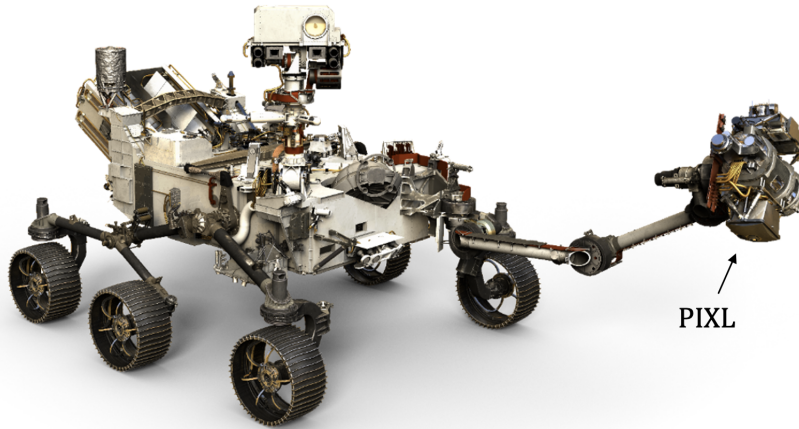


Figure 1: Model of the Mars *Perseverance* rover showing the location of PIXL at the end of the robotic arm.

Spectrometer (APXS) to improve placement proximity, particularly when the target surface is unconsolidated and/or potentially poses a deployment hazard (VanBommel et al., 2019b).

This paper extends the concept of adaptive rover data collection to compositional spectroscopic analysis. Specifically, we describe the adaptive data collection algorithms used by the Planetary Instrument for X-ray Lithochemistry (PIXL), a rastering X-ray fluorescence spectrometer onboard the Mars *Perseverance* rover (Allwood et al., 2020). PIXL’s onboard adaptive sampling procedures perform a simple real-time analysis of acquired spectra, optimizing its limited acquisition time budget to focus on any features of scientific interest that are discovered during data collection. This gathers higher fidelity data from targets of interest that were not anticipated, and which — due to the challenges of instrument placement or the need to move the rover to another location — may not be measured again. At the time of this writing, PIXL’s adaptive sampling capability has been operating on Mars for over 951 sols (martian days), with over 52 scans analyzed. To our knowledge, it represents the first case of autonomous decision-making through compositional analysis performed by a spacecraft on another planet.

We first present an overview of the instrument and the onboard data analysis approach. We then discuss the formulation and testing of rules defining targets of interest. We then describe results and the performance of actual scans conducted on rocks on the surface of Mars.

1.1. The Planetary Instrument for X-ray Lithochemistry (PIXL)

PIXL is an X-ray spectrometer carried by the Mars *Perseverance* rover, mounted on the turret at the end of the rover’s robotic arm, shown in Fig. 1. PIXL’s primary science goal is to gather textural and geochemical contextual data useful for interpreting the geologic history of rocks encountered by the rover, and especially those collected for return to Earth as part of the planned Mars Sample Return. PIXL observations have informed interpretations of the igneous emplacement history of Jezero crater floor rocks and their subsequent histories of alteration by water (Liu et al., 2022; Tice et al., 2022; Farley et al., 2022; Sun et al., 2023). PIXL is designed to autonomously scan the surface of rocks in a pattern spanning up to several centimeters in breadth and width and over a spectral energy range up to 28 keV. This enables the detection of many elements with atomic masses greater or equal to that of Na that are commonly found in rocks and minerals. PIXL’s nominal analytical spot size is 120 μm full width at half maximum (FWHM) at 8 keV, which is roughly the same order of magnitude of the diameters of mineral and rock grains typically observed in sandstones and fine-grained igneous rocks (Allwood et al., 2020).¹

The majority of scans are conducted as follows. An abrasion tool (Moeller et al., 2021) is used to first expose a flat section of sub-surface rock, as shown in Fig. 2. The following sol before sunset the rover arm positions PIXL over the target at a stand-off distance of 25.5 mm, as shown in Fig. 3. The scan is then conducted overnight. The scan begins and then follows a snake-like raster pattern. At each step in the scan, the struts of PIXL’s hexapod move to place PIXL

¹PIXL’s spot size is energy dependent: X-ray excitation and collection areas increase for lower Z elements; i.e., Fe=140 μm FWHM vs Na=230 μm FWHM (Tice et al., 2022).



Figure 2: Preparations for the PIXL scan on sol 294 (Quartier). Most PIXL scans (about 60%) have been conducted on an abraded patch that exposes the sub-surface of the rock (an additional 32% are on natural surfaces and 8% on regolith). In this example an abraded patch of 50-mm diameter and approximately 7-mm deep is produced using the Sampling and Caching Subsystem (Moeller et al., 2021). This patch has been cleared of dust to roughly 40-mm diameter using the Gas Dust Removal Tool. The PIXL scan on sol 294 is 7x7 mm (placement not shown), about one seventh the diameter of the abraded patch, and has 3299 points spaced 0.125 mm apart.

at a new location above the surface of the target. An X-ray spectrum is then recorded, typically with a short 10-s dwell (integration) time. After acquiring the spectrum, the hexapod advances the PIXL sensor to the next physical location to repeat the process.

Each PIXL raster image comprises several thousand short dwells, in total lasting 10 to 14 hours depending on the scan size, so time is the primary limiting resource on the size of these datasets. Long dwells, greater than 10 s, are always desirable to accumulate more photons and improve the measurement precision, but it is not generally possible to program an entire raster of long dwells due to time constraints. Moreover, surfaces can be quite heterogeneous, with small minerals and features of interest distributed unevenly throughout the target matrix. Operators cannot anticipate where the most interesting features will be discovered or place the instrument with sufficient accuracy to know which spectra should be lengthened. This motivated the team to develop PIXL’s adaptive sampling capability.

1.2. Adaptive Sampling

Adaptive sampling aims to trigger longer dwells dynamically in near real-time by interpreting features in the PIXL spectra to identify compositionally valuable locations. In this fashion, PIXL optimizes its finite data collection time, allocating longer dwells at locations of high scientific value.

With adaptive sampling activated, PIXL conducts a brief analysis after acquiring each spectrum before moving to the next location. The raw spectra from each of PIXL’s two detectors are summed together, quantized in 4096 channel bins. They are then re-binned into 22 *pseudo-intensities* each corresponding to spectral bands spanning peaks of interest in the spectrum, as illustrated in Fig. 4. The pseudo-intensities are background-subtracted and then normalized by the background to adjust for the count-rate. The background estimation is performed via a peak-removed non-parametric smoothing algorithm originally from Van Grieken and Markowicz (2001), adapted to PIXL by W. T. Elam (Thompson et al., 2015). These pseudo-intensities are proxies for the strength of the X-ray signal intensity for each element. Figure 4 illustrates the pseudo-intensity definitions used by PIXL, discussed further in Section 3.2. The onboard software compares the spectrum to a library of trigger conditions, or *rules*, constructed in advance by the science team. If a change or pattern of pseudo-intensities triggers an adaptive sampling rule, then a long dwell is initiated to obtain higher signal-to-noise spectra at that location. Once the long dwell is completed, the hexapods then move PIXL to the next step in the scan, where the process is repeated.² A fixed time is allocated for adaptive sampling so that PIXL

²There are additional parameters that can be set to control the behavior of the adaptive sampling, i.e., the total number of long dwells and details of how the sequence of long dwells is executed; allowing for example two long dwells to occur with each trigger, or forbidding a second trigger to occur immediately after a long dwell.

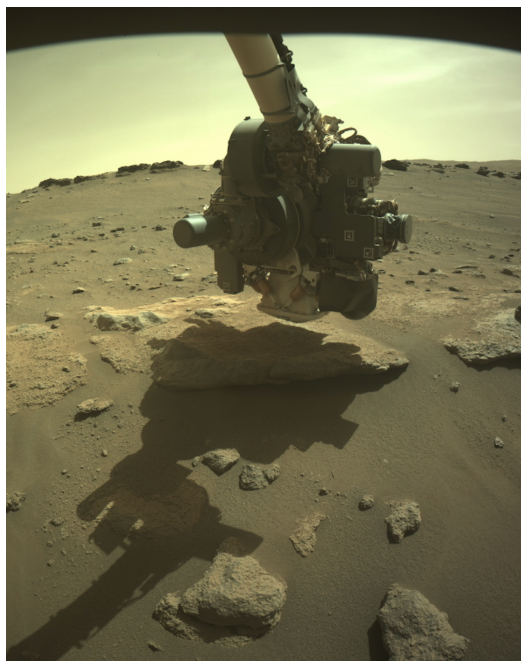


Figure 3: Front Hazcam image of PIXL being placed for an overnight scan on sol 294 (Quartier). The PIXL cover is opened and the robotic arm is used to position the instrument at a stand-off of 25.5 mm from the abraded surface.

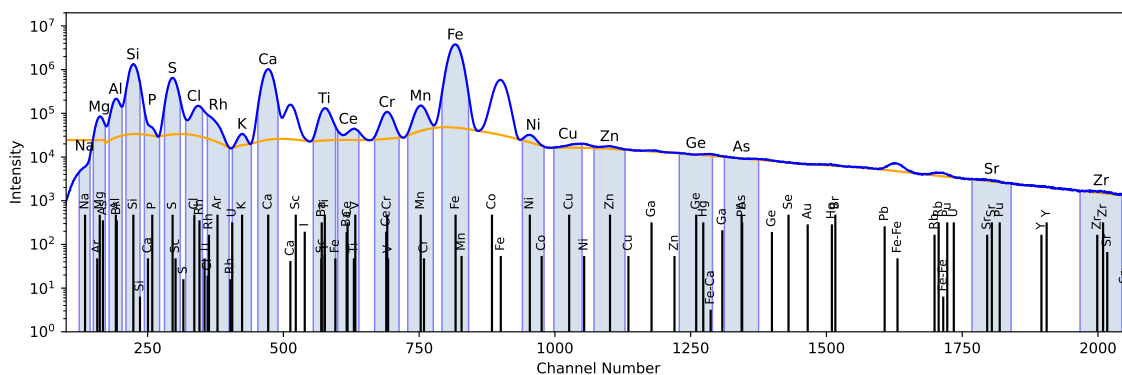


Figure 4: Pseudo-intensity channel boundaries and the locations of major peaks in the spectrum. The upper dark blue line is a plot of the smoothed bulk-sum spectrum of data taken on sol 865 (Dragon's Egg Rock 2). The estimated background is indicated by the orange line. The 22 light-blue vertical bands represent the channels spanned by each of the 22 pseudo-intensities. For reference the locations and relative intensities of common spectral features are indicated by the black vertical lines at the bottom of the plot. Note that the Bremsstrahlung at channel ~ 172 is used as a proxy for the background at lower energies, as discussed by Thompson et al. (2015).

abides by schedule and power constraints imposed by the rover. A commonly used scan is 5×7 mm in area, has 2337 steps, takes about 10 hours to complete, and includes 22.5 minutes for adaptive sampling (45 long dwells of 30 s each).

As currently implemented in PIXL, adaptive sampling doubles the signal-to-noise ratio at selected locations. Long dwells are typically 30-s long, performed in *addition* to the standard 10-s short dwells. The effective total integration time with the additional long dwell is therefore 40 s, which improves the signal-to-noise ratio by a factor of 2, the

square root of the ratio of the respective integration times, $\sqrt{40/10}$. This increased sensitivity not only provides a selective increase in the sensitivity of the instrument but potentially improves the detection of trace elements.

2. Approach

2.1. Dot Product Rules

The adaptive sampling rules we have implemented with PIXL are almost all dot-product rules. These rules use a projection operator to identify pseudo-intensities that are similar to a designated template pattern. Specifically, the rules are defined as reference vectors that are projected onto a vector of pseudo-intensities. If a rule vector and a pseudo-intensity vector are found to be pointing in the same direction (above a threshold value of their dot-product) then the rule is deemed to be satisfied and a long dwell is triggered.

The adaptive sampling flight software (FSW) is used to calculate a normalized dot-product of a rule vector \vec{w} with a pseudo-intensity vector $\vec{\psi}$ and compare it against a threshold β . The formula used by the FSW is as follows:

$$\frac{\vec{w} \cdot \vec{\psi}}{|\vec{w}| |\vec{\psi}|} > \beta, \quad \text{where} \quad -1 \leq \beta \leq 1. \quad (1)$$

Up to 32 rules can be implemented in a single ruleset; each are evaluated sequentially by the FSW.

We have implemented two methods of creating dot-product rules for PIXL: 1) machine learning and 2) ternary compositional diagram analysis. The method of choice depends on whether prior data exists for the targets of interest.

2.1.1. Approach 1: Machine Learning

For the machine learning approach we assume we have many past examples of the compositions of interest for which we want to trigger a long dwell. The general approach is as follows:

1. Create a training database from past examples which lists at each step in a scan (the PIXL Motor Count, or PMC) a number that quantifies how interesting that point is, along with the corresponding pseudo-intensities at that step. The number, a figure of merit, could be either a weight percent (wt%) quantification of a composition or the results of a more complicated expression based on those quantifications.
2. For each composition of interest establish a threshold above which we would like to trigger a long dwell.
3. Write a linear equation as a function of the pseudo-intensities (with as yet unknown coefficients) that sums to 1 for points in the scan above the threshold and sums to -1 for points below the threshold.
4. Solve for the pseudo-intensity coefficients that best satisfy these equations. These coefficients define the rule.
5. If the dot-product of coefficients and pseudo-intensities is greater than zero, then we say the rule is satisfied and a long dwell should be triggered.

We can use Eq. 1 to understand the problem as one of linear classification with a hard threshold (Russell and Norvig, 2020, section 19.6.4). The rule coefficients and pseudo-intensities together provide a linear approximation of a normalized figure of merit q that is evaluated against a normalized threshold β . At each PMC we have an X-ray spectrum and a set of pseudo-intensities. If the rule vector is normalized so that $|\vec{w}| = 1$, we can write the classification hypothesis y_{PMC} as follows:

$$y_{\text{PMC}} = \begin{cases} 1 & \text{if } q_{\text{PMC}} > \beta \\ -1 & \text{if } q_{\text{PMC}} \leq \beta \end{cases}, \quad \text{where} \quad q_{\text{PMC}} = \frac{1}{|\vec{\psi}_{\text{PMC}}|} \sum_i w_i \psi_{i \text{ PMC}}, \quad (2)$$

and $\psi_{i \text{ PMC}}$ is the i th element of the 22-element pseudo-intensity vector $\vec{\psi}_{\text{PMC}}$ recorded at a given PMC. The vector \vec{w} is a set of weights (the rule) that defines a multi-dimensional plane that separates one class of points from all others. If for a given $\vec{\psi}_{\text{PMC}}$ and \vec{w} , y_{PMC} lies above the plane, then the classification hypothesis is 1 and a long dwell is triggered; if it falls below the plane then the hypothesis is -1 and no long dwell occurs.

In practice Eq. 2 will yield tens of thousands of linear equations, one for every individual PMC in the training set. A least-squares regression is used to solve for the weights \vec{w} that best satisfy the set of equations defined by \vec{y}_{PMC} and $\vec{\psi}_{\text{PMC}}$. The authors solve for these equations using a statistical gradient descent algorithm.

It should be noted that machine learning algorithms commonly pre-process the training sets to be normalized with a zero mean. However, this pre-processing is not implemented in the PIXL FSW and the raw pseudo-intensities are used instead.

2.1.2. Approach 2: Analysis of Ternary Compositional Diagrams

There may however be compounds of interest for which no past observations exist, but which can nonetheless be isolated in a ternary compositional diagram. This was our initial approach for formulating dot-product rules for PIXL on the *Perseverance* rover.

A ternary compositional diagram, examples of which are shown in Section 4, illustrates the relative abundances of three materials or compounds found in a sample. The diagram is triangular, and each apex is labeled with one of the three compounds. At the apex the contribution of the compound labeled there is 100%; on the side opposite the apex the contribution is 0%. Regions of interest in a ternary diagram can be isolated as lying above or below a line representing the abundance of one compound relative to the other two. These abundances can be expressed as quantified weight percents, calculated by analysts on Earth using sophisticated modeling software that is not available onboard. However, we found that it is possible to approximate the abundance calculations for specific geologic domains using linear combinations of pseudo-intensities. The general approach is as follows:

1. Create a database from past examples which lists at each step in a scan the weight percent quantification of compositions of interest along with their corresponding pseudo-intensities.
2. Using a least-squares fit, derive linear approximations of the weight percent quantifications as a functions of the pseudo-intensities.
3. Draw a ternary diagram whose contributions are normalized in milli-mols that has 1) the composition of interest at the apex; 2) important distinguishing compositions in the bottom left-hand corner; and 3) a collection of other much less important distinguishing compositions in the bottom right-hand corner.
4. Set a percent threshold for the composition of interest that isolates it from the other two groups.
5. Express as an equation the ratio of the apex divided by the sum of the compositions in all three corners being greater than the threshold.
6. Cross-multiply and re-arrange the equation so that it appears as an linear equation with a threshold of zero.
7. From Step 2 above, substitute for each composition a linear equation in terms of pseudo-intensities.
8. Re-write the linear equation in terms of pseudo-intensities. The coefficients of the pseudo-intensities define the rule.

We used this approach in some of the earliest dot-product rules derived for PIXL, but as the mission progressed and many tens of thousands of PMCs of data were recorded, we re-derived all of the ternary diagram rules as machine-learning rules. The remainder of this paper is devoted to describing our implementation and assessment of our machine learning approach with PIXL.

3. Implementation

3.1. Adaptive Sampling Simulation

We developed a stand-alone adaptive sampling simulation environment based on PIXL FSW.³ This included the adaptive sampling FSW and higher-level sections of FSW that implement the decision-making logic used when PIXL steps through a scan. We extended it to allow previously recorded Mars PIXL data to be re-processed and re-analyzed with new rulesets. The re-processing takes the raw spectra, creates pseudo-intensities based on the ruleset definitions (described below), and then evaluates them to determine where long dwells are triggered.

We validated the simulation environment by having it re-process previous Mars PIXL data using the same rulesets that were on the rover, and demonstrating that it produced the same pseudo-intensities and the same long dwell locations as PIXL did on each scan.

We test new rulesets in simulation with previously recorded Mars data, knowing that the behavior observed in simulation is identical to what would have been observed on Mars had these rules been implemented. Rulesets that produce a large number of True Positives while yielding few False Positives are candidates for implementation.

3.2. Pseudo-intensity Database

The first step in preparing a new ruleset is to create a database of pseudo-intensities. A pseudo-intensity is a representation of part of a spectrum that records the integrated counts under a peak and is optionally background-subtracted

³PIXL's adaptive sampling algorithm was written by D. R. Thompson and integrated within the FSW by M. S. Gilbert, B. J. Bornstein, and R. W. Denise.

Table 1

Pseudo-intensity channel definitions for ruleset 230328. All of the pseudo-intensities are background-subtracted and normalized except for Rh and Zr. The Rh signature originates from the PIXL X-ray tube anode, and its pseudo-intensity is used as a measure of the background, thus the background is not subtracted in this case. The background at Zr is very noisy and would corrupt the Zr pseudo-intensity if background-subtraction and normalization were used, so both are disabled.

Element	Center (keV)	Start Channel	End Channel	Subtract Background	Normalize
Na	1.04	124	144	1	1
Mg	1.25	150	172	1	1
Al	1.49	179	203	1	1
Si	1.74	210	236	1	1
P	2.01	244	272	1	1
S	2.31	281	310	1	1
Cl	2.62	320	351	1	1
Rh	2.70	360	400	0	1
K	3.31	406	441	1	1
Ca	3.69	453	490	1	1
Ti	4.51	555	596	1	1
Ce	4.84	600	639	1	1
Cr	5.41	668	713	1	1
Mn	5.90	729	776	1	1
Fe	6.40	792	841	1	1
Ni	7.48	940	980	1	1
Cu	8.05	998	1050	1	1
Zn	8.64	1072	1129	1	1
Ge	9.89	1229	1290	1	1
As	10.54	1312	1375	1	1
Sr	14.17	1768	1840	1	1
Zr	15.75	1967	2044	0	0

and/or normalized. These pseudo-intensities are created when data is processed in the simulation environment. The database is created using a dummy ruleset which includes placeholder rule coefficients, the channel boundaries of the pseudo-intensities, and instructions whether background-subtraction and/or normalization is used.

A single 4096-channel X-ray spectrum is approximated by a set of 22 pseudo-intensities. The quantities that define a pseudo-intensity are as follows:

1. Pseudo-intensity name, such as "Na", "Mg", etc.
2. Peak location (keV), converted to a detector channel number.
3. Peak width (keV), with the peak location converted to starting and ending channel numbers.
4. Whether background subtraction is used or not, denoted by a 1 or 0 respectively.
5. Whether the pseudo-intensities are normalized or not, denoted by a 1 or 0 respectively.

Table 1 lists the parameters that define the pseudo-intensities at the time of writing. Figure 4 shows these pseudo-intensity bands superimposed on a bulk spectrum of data from sol 865. The peak widths are proportional to the square-root of the peak channel number; in some cases the the start and end channels were adjusted manually, based on inspection of the bulk spectra from past data. The relationship between energy in keV and channel number for detector A is given by the following equation, where y is the energy in eV and x is the channel number.⁴

$$y = 7.86x - 18.5 \quad (3)$$

The pseudo-intensity database is created by re-processing past Mars PIXL data according to these definitions.

⁴The adaptive sampling algorithm uses the sum of counts from detectors A and B. Although the calibration for detector B is slightly different, for the purpose of defining the pseudo-intensity boundaries this difference is of no consequence. These calibrations will change slowly over the mission and must be periodically updated.

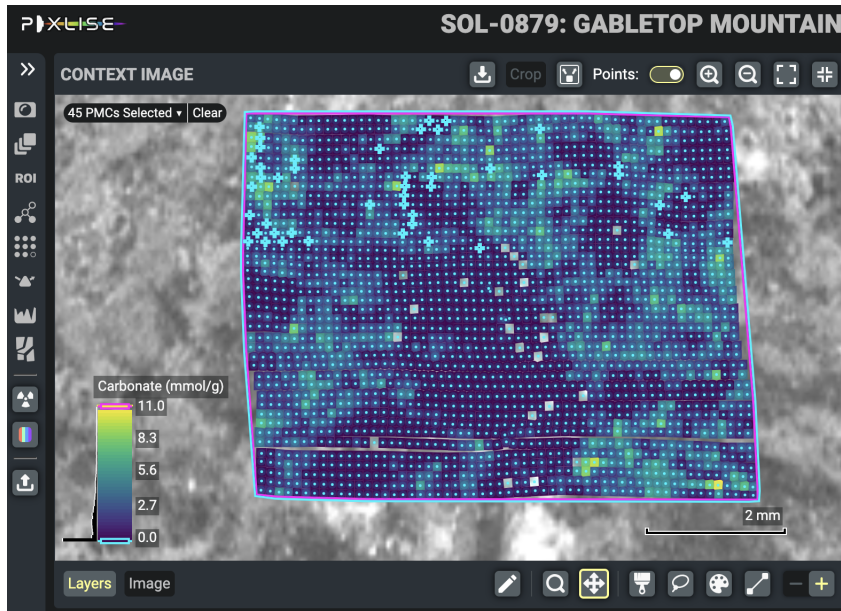


Figure 5: PIXLISE view of carbonates detected on sol 879 (Gabletop Mountain). Shown here is a compositional map of carbonates derived from PIXLISE "expressions". The expressions are equations that can use counts from PIXL's two detectors to estimate weight percents of compositions of interest while taking into account the effects of diffraction. The grey-colored points are where divide-by-zero errors have occurred and should be ignored.

3.3. Quantification Database

The second step in preparing a new ruleset is to create a database of oxide weight percent quantifications from past scans. Shortly after a scan has been downlinked from the rover, it becomes available to the science team in PIXLISE (Nemere et al., 2024), a data analysis and visualization tool. Within PIXLISE, a member of the PIXL science team runs the PIQUANT algorithm (Heirwegh et al., 2022, 2024) to quantify the presence of oxides found at each PMC in that scan. PIXL has two X-ray detectors (designated as detector A and detector B), and PIQUANT is configurable to process data separately from each detector or with both detectors combined. Because the default configuration for adaptive sampling is to analyze the combined (A + B) data, we catalog *combined* quantifications produced by PIQUANT.

However, quantifications for carbonates are treated differently. Unlike most mineral compositions which are estimated solely by the PIQUANT algorithm, carbonates are estimated through higher-order "expressions" in PIXLISE. The expressions for carbonates use the PIQUANT quantifications for each separate detector but also attempt to remove the effects of diffraction by comparing detector counts. Moreover the expressions for carbonates may differ from one scan to another depending on the composition of the substrate. We catalog the results of the agreed-upon expressions separately from the routine PIQUANT quantifications. An example of a carbonate map is shown in Fig. 5.

3.4. Machine Learning

The quantification database along with the pseudo-intensity database are mathematically compared to derive our adaptive sampling rules.

3.4.1. Creation of Training Datasets

The machine learning training set for a compound of interest is created using thresholds of weight percent for that compound. If in past scans the weight percent at a given PMC exceeds the threshold, then we declare that the compound is present; conversely if it falls below the threshold, then we declare the compound is absent.

The coefficients, and therefore the performance, differ depending on the thresholds that are applied to create the training sets. Generally, the lower the threshold, the higher the True Positive Rate. However, the number of False Positives can change significantly with even a small change in threshold in the training set. Therefore to arrive at an acceptable set of coefficients, multiple training sets are created that each have slightly different thresholds across some

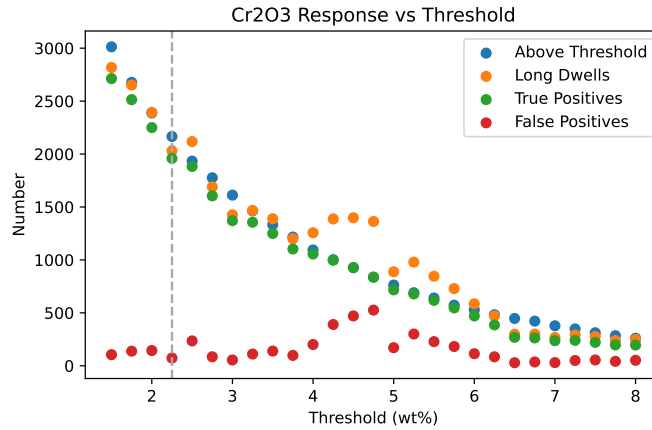


Figure 6: Cr_2O_3 rule performance vs threshold. The performance of 27 different candidate Cr_2O_3 rules are shown, with each rule using a different weight percent threshold. The number *Above Threshold* are the number of PMCs in the training set where the weight percent of Cr_2O_3 exceeds the threshold wt%. The number of *Long Dwells* is the total number of dwells that were triggered by the rule: the sum of the *True Positives* and *False Positives*. The *True Positives* are the number of long dwells where the weight percent was above the threshold. The *False Positives* are the number of long dwells where the weight percent was below the threshold. The rule coefficients for Cr_2O_3 were chosen from the case corresponding to a threshold of 2.25 wt%, denoted by the vertical dashed grey line, where the True Positives were numerous and the False Positive were few.

nominal range. For example, we might create 20 training sets spanning 3.0 to 8.0 wt% in 0.25 wt% steps. We then choose a training set that provides acceptable performance. The approach is as follows:

1. Define which datasets (sols) contribute to the training: specify the most recent sol to be included and any sols to be excluded.
2. Establish the minimum and maximum thresholds to be tested and the number of training sets in between that will be generated.
3. For each quantity of interest and for each threshold create a training set. The training set is a matrix with each row corresponding to a different PMC. The first column in the matrix has the value 1 or -1, depending on whether or not based on the analysis a long dwell should be triggered at that PMC. The subsequent 22 columns in each row list the corresponding calculated pseudo-intensities.

These files are passed along to a separate program, described below, that solves for the rule coefficients.

3.4.2. Classification by Stochastic Gradient Descent

Each training set is processed in the following manner to derive rule coefficients:

1. Define which (if any) of the 22 pseudo-intensities should be ignored in the solution.
2. Read in the training data, as described previously.
3. Delete from the matrix of equations any pseudo-intensities that should be ignored.
4. Solve for coefficients of a linear least-squares fit to derive the best solution for the matrix of equations. In our implementation we use a Stochastic Gradient Descent approach, `sgdClassifier`, from the scikit-learn Python library (Pedregosa et al., 2011).
5. Evaluate various different loss functions for Stochastic Gradient Descent (hinge, log loss, perceptron, etc.) to see which works the best. Coefficients of the solution with the best performance are retained, as described in the following section.
6. Coefficients of 0.0 are inserted as part of the solution to correspond with the pseudo-intensities that were ignored.

3.4.3. Evaluation of Coefficients

We evaluate the performance of a ruleset by using it in simulation to reprocess the same data it was trained on — all the available Mars PIXL data up until that date. The long dwells that are triggered are then compared against the quantifications and thresholds for each compound. As an example, Fig. 6 shows the performance of different candidate Cr_2O_3 rules, each created with training sets having different weight percent thresholds. At each PMC if the dot-product between the pseudo-intensity vector and the vector of rule coefficients is a number greater than zero (see Eq. 1) then the rule would have triggered a long dwell at that location. The long dwells, true positives, and false positives are then evaluated. A ruleset is then chosen in a heuristic fashion amongst candidate rules that have a large number of True Positives with an acceptable number of False Positives.

3.5. Ruleset 230328

This paper describes the performance of ruleset 230328,⁵ which was first used on the rover on sol 847 (Lake Helene). This new ruleset was developed primarily to improve the performance of a Zr rule, which was designed to trigger on 7σ changes in the Zr pseudo-intensity. We took the opportunity to revise the dot-product rules for the detection of the other phases of interest identified by the science team (see Section 5.1) including carbonates, spinel minerals (identified by enrichments in Cr_2O_3 and TiO_2), manganese (MnO), and phosphate minerals (referred to as "phosphates" and identified by enrichments in P_2O_5). We also included a new rule to detect 6σ changes in Cu. A partial history of adaptive sampling use on the rover is provided in Table 2. Additional details are provided in Table 3.

In the previous ruleset (220424) the Zr rule had been triggering on noise introduced by a noisy background-subtraction and normalization. By omitting the Zr background-subtraction and normalization in ruleset 230328 (see Table 1), the simulated performance was greatly improved. In the data presented in this paper, however, there was never an opportunity for this rule to trigger. Nonetheless, simulations show that the Zr rule would have triggered correctly on sol 865 (Dragon's Egg Rock 2) at PMCs 1277, 1526, and 2044, but the adaptive sampling budget of 45 long dwells had been exhausted on that scan at PMC 1254. The PIQUANT-derived combined weight percents of ZrO_2 at those PMCs are 0.74 wt%, 1.09 wt%, and 0.71 wt% respectively.

These new rules were based on scan data from sols 125 through 751. This included scans not only on abraded surfaces, but also on natural surfaces and regolith. The pseudo-intensity for Zr was ignored in the creation of these dot-product rules; the rule coefficient for Zr in each case was set to 0.0. The resulting coefficients for the dot-product rules are given in Table 4.

The coefficients shown in Table 4 seem intuitively correct. The largest coefficient of the Cr_2O_3 rule belongs to the Cr pseudo-intensity. Similarly the largest coefficient of the P_2O_5 and MnO rules belong to the P and Mn pseudo-intensities respectively, as one might expect. The largest coefficient of the TiO_2 rule is Ce; the primary analytical Ce line ($L\alpha$ at 4.84 keV) overlaps the tail of the secondary Ti analytical line ($K\beta$ at 4.93 keV), thus pseudo-intensities of Ce and Ti are intertwined and positive correlations for both with Ti concentration is expected (see for example Fig. 4). The carbonate rule is somewhat inscrutable. It does not have a single positive coefficient that stands out from the others, but rather has positive values of a similar magnitude distributed across Ge, Mn, Na, K, and Mg, and negative coefficients (i.e., unlike carbonate) distributed across Ni, Cu, Ce, As, Al, and Zn.

4. Results: Performance Assessment

The performance assessment required reprocessing data on the ground for all data taken from sols 847 to 921 inclusive. The FSW on PIXL does not report which rule in the ruleset was triggered, only that a long dwell occurred. To understand which rule corresponded to which long dwell, the Mars data were re-processed using ground-based software that would run each rule separately rather than all at once. These results were filtered to points within the scan where adaptive sampling was active, i.e. points within the total budget and points not excluded because of other sampling parameters. The number of long dwells from each rule that were triggered between sols 847 and 894 is shown in Table 5. The PMCs associated with those long dwells are provided in the Supplemental Material. The results are shown in Figures 7, 8, and 9. For the comparisons, long dwells caused by other rules are excluded from these plots.

Each observation typically used an adaptive sampling budget of 45 long dwells, or approximately 22.5 minutes added to the total scan time. The plots show a comparison between the points that were sampled with short dwells and those points where long dwells were triggered by the ruleset.

⁵The ruleset number is a year-month-date format (YYMMDD) denoting when the ruleset was completed: March 28, 2023.

Table 2

PIXL scan and adaptive sampling parameters used on Mars from sol 450 to 921. As can be seen, adaptive sampling has been used routinely. Adjustable parameters include the short dwell time (Norm), the long dwell time (Dwell), and the total number of long dwells allowed (Budget). The total number of long dwells that were triggered (Dwells) is also listed.

Sol	Target Name	Samples	Surface Type	Ruleset	Norm (s)	Dwell (s)	Budget	Dwells
0921	Amherst Point 2	2337	Abraded	230328	10	30	45	45
0920	Amherst Point 1	2337	Abraded	230328	10	30	45	45
0894	Thunderbolt Peak 2	2581	Abraded	230328	10	30	45	45
0887	Thunderbolt Peak 1	2581	Natural	230328	10	30	60	60
0880	Gabletop Mnt 2	2581	Abraded	230328	10	30	45	45
0879	Gabletop Mnt 1	2337	Abraded	230328	10	30	45	45
0874	Pilot Mountain	1377	Natural	230328	10	30	45	45
0865	Dragon's Egg Rock 2	2581	Abraded	230328	10	30	45	45
0860	Dragon's Egg Rock	2337	Abraded	230328	10	30	45	45
0852	Lake Haiyaha 2	2581	Abraded	230328	10	30	45	45
0851	Lake Haiyaha 1	2337	Abraded	230328	10	30	45	18
0847	Lake Helene	2337	Natural	230328	10	30	45	28
0811	Ouzel Falls 3	3333	Abraded	220424	10	30	90	88
0790	Ouzel Falls 2	825	Abraded	220424	10	30	10	10
0789	Ouzel Falls	2337	Abraded	220424	10	30	45	25
0782	Solitude Lake	2337	Abraded	220424	10	30	45	42
0781	Pipit Lake	2337	Natural	220424	10	30	45	10
0751	Solva 2	3333	Abraded	220424	10	60	30	30
0747	Solva	2337	Abraded	220424	10	30	45	16
0711	Cavetown	2337	Natural	220424	10	30	45	11
0698	Utz Gap	2581	Natural	220424	10	30	45	45
0618	Uganik Island 3	121	Abraded	-	60	0	0	0
0617	Uganik Island 2	1681	Abraded	221003	10	60	45	45
0614	Uganik	3333	Abraded	220424	10	30	28	28
0601	Marmot Bay 2	1653	Regolith	221003	10	30	45	45
0600	Marmot Bay	225	Regolith	221003	10	30	25	11
0598	Topographers Peak	1681	Regolith	220424	10	30	45	17
0589	Ursus Cove 2	225	Regolith	221003	10	30	40	13
0577	Ursus Cove	363	Regolith	-	10	0	0	0
0573	Novarupta 3	1681	Abraded	220424	10	30	100	100
0570	Novarupta 2	3333	Abraded	220424	10	30	100	100
0567	Novarupta	1653	Natural	220424	10	30	150	1
0560	Chiniak Offset 2	1653	Natural	220424	10	20	135	20
0558	Chiniak Offset	363	Natural	220424	10	30	15	15
0507	Berry Hollow 2	1653	Abraded	220424	10	30	45	11
0505	Berry Hollow	3333	Abraded	220424	10	30	45	22
0490	Thorton Gap 2	363	Abraded	220424	10	30	10	5
0484	Thorton Gap	3333	Abraded	220424	10	30	45	45
0480	Shop Hollow	1681	Natural	220424	10	30	45	18
0463	Pignut Mountain	363	Natural	220424	10	40	15	0
0450	Rose River Falls	242	Natural	220424	10	30	30	8

The rule performance is evaluated by showing the weight percent of compounds at points that triggered long dwells versus the weight percent of points that did not, subject to the filtering described above. The results are also shown within ternary compositional diagrams illustrating the separation of long dwells from normally sampled points across a range of compounds.

Table 3

Chronology of adaptive sampling ruleset uplinks.

Uplink Sol	Ruleset	Description
816	230328	Cr ₂ O ₃ , TiO ₂ , P ₂ O ₅ , Carbonates, MnO, Cu, Zr
586	221003	Line scan dot-product
424	220424	Cr ₂ O ₃ , TiO ₂ , Phosphates, Carbonate Fe Mg Mn, Carbonate Ca, Mn, Zr

Table 4

Coefficients for ruleset 230328. Each column lists the rule coefficients for different dot-product rules in the ruleset. Coefficients are shown for rules for carbonates, Cr₂O₃, TiO₂, P₂O₅, and MnO. The percentages associated with the rule denote the threshold used in the training set. For example, the rule designed to detect Cr₂O₃ used a training set to detect 2.25 wt% or greater. The coefficients listed here are rounded to 5 decimal places for ease of inspection; the coefficients uploaded to the rover were exactly those output from `sgdClassifier`, some to 9 decimal places. The largest coefficients for each rule, those that principally determined whether the rule will trigger or not, are shown in bold text. (Note that the Cu and Zr rules are not dot-product rules and therefore have no coefficients listed here; they trigger from 6σ and 7σ changes in their pseudo-intensities, respectively.)

Pseudo-intensity	Carbonates 4.58 wt%	Cr ₂ O ₃ 2.25 wt%	TiO ₂ 3.00 wt%	P ₂ O ₅ 3.50 wt%	MnO 2.25 wt%
Na	0.15851	0.10316	0.24538	0.04665	-0.02502
Mg	0.11073	0.00339	-0.22796	-0.15820	-0.11670
Al	-0.17406	-0.20837	-0.07513	0.01868	-0.15117
Si	-0.05041	-0.01588	-0.03850	-0.09805	-0.02721
P	-0.10058	0.02888	-0.10321	0.95600	-0.03069
S	-0.10094	-0.04763	-0.06461	-0.02092	-0.05203
Cl	0.00052	0.03007	-0.06779	-0.02470	-0.00791
Rh	-0.03586	-0.15829	-0.05199	0.00620	-0.10985
K	0.12458	-0.20392	-0.27578	0.14737	-0.28563
Ca	-0.03539	-0.05314	-0.09512	0.01899	-0.02749
Ti	-0.10685	0.17638	0.38019	-0.02098	-0.10216
Ce	-0.28577	-0.13606	0.65148	0.01003	0.01213
Cr	-0.06706	0.86775	0.05481	-0.02576	-0.09002
Mn	0.17368	-0.17072	-0.14616	-0.11525	0.91098
Fe	0.03227	-0.12742	-0.00340	-0.00395	-0.03076
Ni	-0.51381	-0.06813	-0.24518	-0.07940	-0.02706
Cu	-0.51252	0.03720	-0.24197	-0.05996	-0.09403
Zn	-0.16297	0.06582	0.11837	-0.03024	0.03531
Ge	0.28414	0.09956	-0.18721	0.01618	0.05607
As	-0.28140	0.06219	-0.11002	-0.01235	-0.01691
Sr	-0.02405	-0.00890	-0.01712	-0.00288	-0.01663
Zr	0.00000	0.00000	0.00000	0.00000	0.00000

4.1. Phosphate Rule

The results for the phosphate rule are shown in Fig. 7. One can see from inspection that the rule performs well. The separation of points in the ternary diagram is very clean. Only a few long dwells have anomalously low weight percents of P₂O₅, due to the overlapping Ca escape peak and high-Ca within the P pseudo-intensity band at these points.

4.2. Cr-Ti Spinel Rules

Results for the Cr₂O₃ rule are shown in Fig. 8. All of the highest weight percent points are captured by adaptive sampling, and only a small number of long dwells are triggered with anomalously low weight percents. Over the range of sols for which the new ruleset was used, there was very little TiO₂ detected, and therefore these results are not shown.

Table 5

Number of long dwells per rule from Sol 847 to 921 with ruleset 230328. The PMCs associated with each long dwell are provided in the Supplemental Material.

Sol	Target Name	Surface	Carbonates	Cr ₂ O ₃	TiO ₂	P ₂ O ₅	MnO	CuO	ZrO ₂	Dwells
0921	Amherst Point 2	Abraded	10	34	0	0	0	1	0	45
0920	Amherst Point 1	Abraded	6	38	0	0	0	1	0	45
0894	Thunderbolt Peak 2	Abraded	32	13	1	0	0	0	0	45
0887	Thunderbolt Peak 1	Natural	40	17	2	0	0	1	0	60
0880	Gabletop Mnt 2	Abraded	5	33	0	2	1	5	0	45
0879	Gabletop Mnt 1	Abraded	29	13	2	1	0	2	0	45
0874	Pilot Mountain	Natural	31	6	5	0	0	3	0	45
0865	Dragon's Egg Rock 2	Abraded	0	16	9	28	0	0	0	45
0860	Dragon's Egg Rock	Abraded	0	2	4	41	0	0	0	45
0852	Lake Haiyaha 2	Abraded	14	29	0	2	0	0	0	45
0851	Lake Haiyaha 1	Abraded	0	7	0	1	0	10	0	18
0847	Lake Helene	Natural	0	7	21	0	0	0	0	28

Table 6

Evaluation of rule classifications. True Positives (TP), False Negatives (FN), True Positive Rate (TPR = TP/(TP+FN)), False Positives (FP), True Negatives (TN), and False Positive Rate (FPR = FP/(TP+FP)) are listed below as a function of ruleset.

Rule	TP	FN	TPR (%)	FP	TN	FPR (%)
Carbonates 4.58 wt%	68	488	12.2	85	12732	0.66
Cr ₂ O ₃ 2.25 wt%	126	2	98.4	19	13332	0.14
TiO ₂ 3.00 wt%	25	4	86.2	31	13330	0.23
P ₂ O ₅ 3.50 wt%	54	4	93.1	22	13330	0.16
MnO 2.25 wt%	1	1	50.0	0	13333	0.0

4.3. Carbonate Rule

Qualitatively, through inspection of the results in PIXLISE, the carbonate rule appears to perform well, though its true positive rate is only 12.2%. As can be seen in the ternary plot of Fig. 9, the rule indeed isolates carbonates as expected. Compared to the other rules it triggers over a broader range of weight percent, above and below the threshold.

This discrepancy reflects the fact that PIXL does not directly observe characteristic fluorescence X-rays from C; the abundance of carbonate minerals is therefore inferred from PIXL spectra using a multi-step process using the separate spectra from detectors A and B. The adaptive sampling algorithm, on the other hand, uses the summed data from both detectors. The expressions on which the training was based therefore have access to information that is hidden from the adaptive sampling algorithm. It is thus remarkable that a machine-learning based approach using a combined pseudo-intensity dataset is able to reproduce a classification based on complete spectra/quantifications from the separate detectors and expert human mineral classifications.

It is also worth noting that there are multiple types of carbonate, mixed with various mineral compositions observed on natural and abraded surfaces, that were included in the training set. The resultant rule was therefore the result of a heterogeneous mixture of data.

4.4. Discussion: Performance Assessment

As can be seen in Table 6, across the more than 13,300 points sampled in scans from sol 847 to 921 inclusive, the True Positive Rate (TPR) is above 86% for the Cr₂O₃, TiO₂, and P₂O₅ rules, and about 12% for the carbonate rule. The MnO rule had one True Positive and one False Positive, thus a TPR of 50%. For every rule the False Positive Rate was below 0.7%.

It should not be surprising that some long dwells are triggered against samples whose weight percent falls below the threshold. The dot-product rules are trained using training sets whose members have a weight percent for that compound that exceeds a specified threshold, however the dot-product and the pseudo-intensities are all *normalized*, and so the rules trigger against a pattern of pseudo-intensities, not a weight percent.

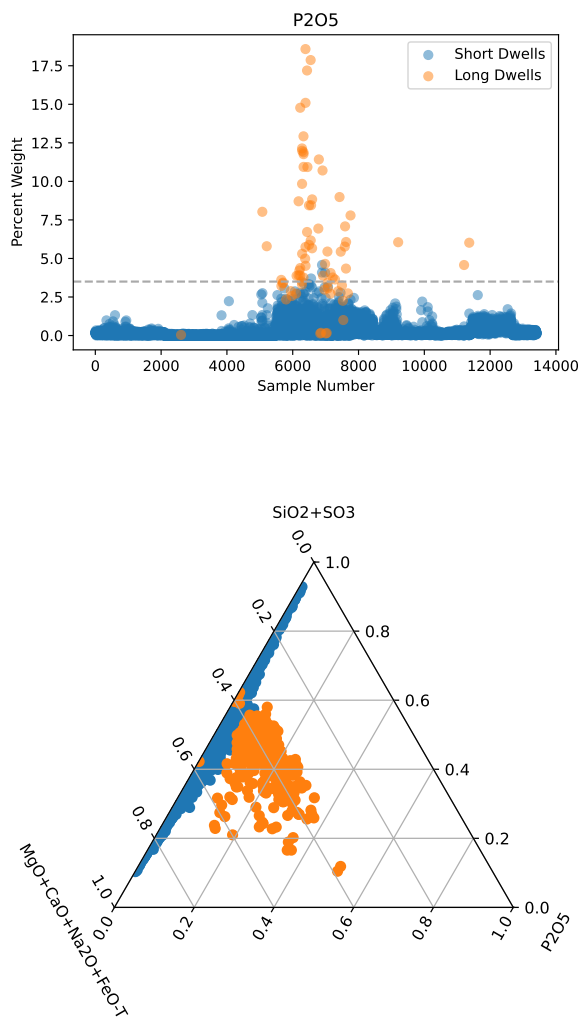


Figure 7: P_2O_5 rule with a 3.5 wt% threshold. The plotted data show 54 true positives, 22 false positives, and 4 false negatives, yielding a true positive rate of 93.1% and a false positive rate of 0.16% (see Table 6). At a small number of points there was a strong Ca escape peak within the P pseudo-intensity band, causing the phosphate rule to trigger when there was very little phosphorus.

More importantly, the pseudo-intensities are each defined across a band of X-ray energies, sometimes spanning spectral lines of more than a single compound. As noted previously, the presence of a strong Ca signature, for example, might cause the P_2O_5 rule to trigger.

Diffraction from the target sample is another possible confounding factor (Tice et al., 2022). The X-ray diffraction effects recorded in PIXL spectra are due to the properties of additive Bragg scattering of the PIXL source X-rays when they encounter crystal lattice planes in mineral materials. Diffraction can cause spurious enhancements of pseudo-intensities and the erroneous triggering of rules. Although this is a known issue, diffraction has not had a noticeable impact on the performance of the adaptive sampling algorithm.

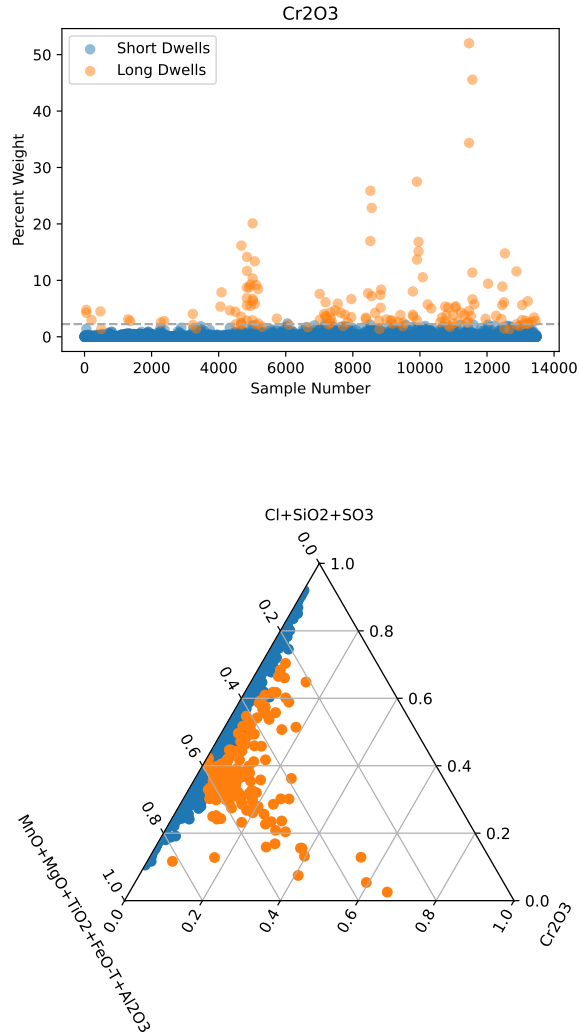


Figure 8: Cr_2O_3 rule with a 2.25 wt% threshold. The plotted data show 126 true positives, 19 false positives, and 2 false negatives, yielding a true positive rate of 98.4% and a false positive rate of 0.14%.

5. Science Assessment

5.1. Scientific Motivation

5.1.1. Improve quantity and quality of data on smaller, rarer phases

Longer dwells improve the quantity and quality of data on smaller, rarer phases of interest. The adaptive sampling rules currently on the Mars 2020 rover have been designed to trigger longer dwells on minor and accessory phases of interest (phases that comprise <10% of a rock). These phases include: phosphate minerals, spinels, Zr-minerals (mainly zircon [ZrSiO_4] and/or baddeleyite [ZrO_2]), Mn-enrichments, and Cu-enrichments.

Phosphate minerals, spinels, and Zr-minerals are relatively common minor and accessory phases in martian rocks (McCubbin et al., 2016; Herd et al., 2018; Udry et al., 2020), but their sizes are often close to, or much less than PIXL's spot size of $\sim 120 \mu\text{m}$ FWHM at 8 keV (with larger spot sizes at lower energies, see Section 1.1). Martian phosphate and spinel minerals typically range in size from 10s to 100s of μm in diameter (i.e., McCubbin et al. 2016; Goodrich

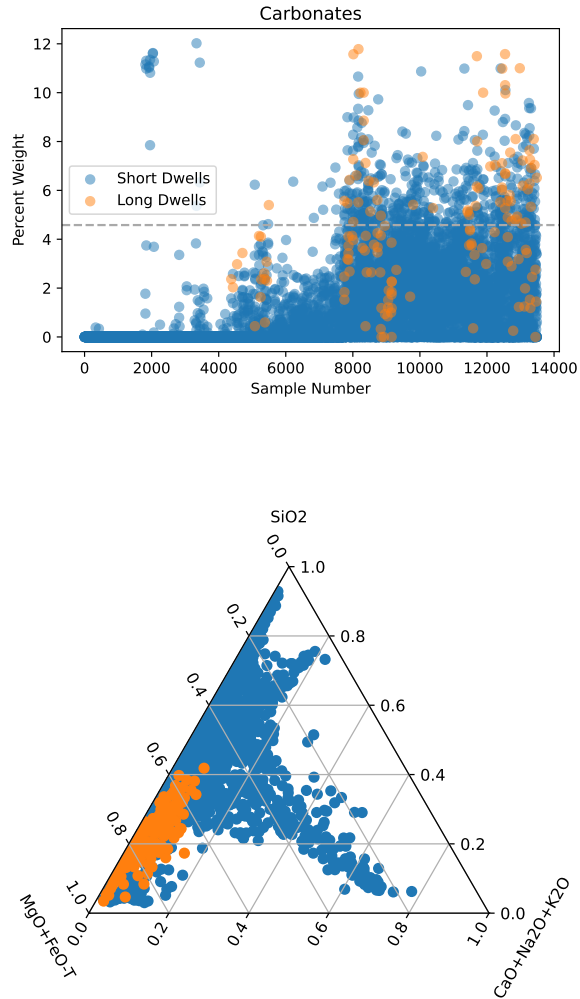


Figure 9: Carbonate rule with a 4.58 wt% threshold. The plotted data show 68 true positives, 85 false positives, and 488 false negatives, yielding a true positive rate of 12.2% and a false positive rate of 0.66%.

et al. 2003), while Zr-minerals are most often $<10\ \mu\text{m}$ (Herd et al., 2018). Due to their small volume and small sizes, even high resolution PIXL maps will typically only include a limited number of accessory phase analyses. In order to ensure good quality data are collected from these rare minerals, we target them with adaptive sampling.

Manganese is of special interest as a major constituent for several reasons. However, it is an element that is more typically found at a minor concentration level of 0.01 to 0.02 times the concentration of Fe, for which it can substitute at a low level in common minerals such as olivine and pyroxene, including in martian meteorites (Papike et al., 2009). However, when Mn is found at higher levels than these, the minerals involved may be rare but highly important to the interpretation of the geochemical sample being analyzed. On Mars, past Mn-enrichments have been associated with sulfates (Arvidson et al., 2016; Lanza et al., 2014), with Cl-rich coatings (Berger et al., 2019; VanBommel et al., 2022), and within phosphate minerals (Treiman et al., 2023; VanBommel et al., 2023). The minerals involved have been interpreted to indicate a possible higher oxidizing environment on Mars (Lanza et al., 2015) or a salt precipitation sequence (Berger et al., 2022). Manganese alteration minerals can provide important clues to past environmental

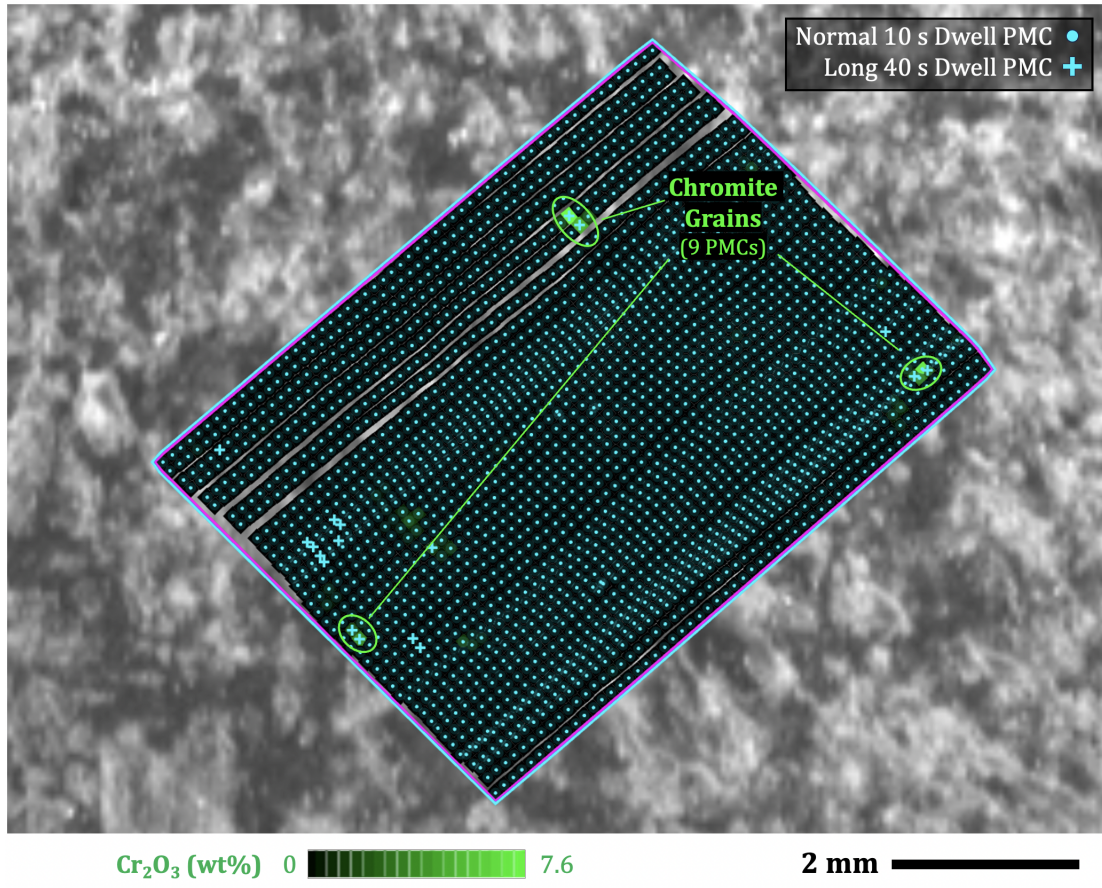


Figure 10: 5 × 7 mm PIXL scan of target Lake Haiyaha (sol 851) displaying elemental abundances of Cr_2O_3 in green. The scan only contains 3 Cr-rich grains (chromites) comprising 9 PMCs total (0.4% of the map scan [9 PMCs/2346 PMCs]). The Chromite-bearing PMCS are defined here as PMCs with >2 wt% Cr_2O_3 .

conditions, and hence aid in the inference of environments in the past and whether they would be consistent with an enhanced or degraded level of habitability.

Copper has been found at enhanced levels in Gale Crater, Mars (Payré et al., 2019; VanBommel et al., 2019a; Goetz et al., 2023; Forni et al., 2024). When olivine weathers, it may liberate its ~ 100 ppm Cu (De Vos et al., 2006). Copper is mobile under oxidizing, acidic conditions, especially at pH of 5.0 to 6.0, and has an affinity for organic matter (De Vos et al., 2006). Copper is an essential trace element for all known life forms. Hence, its bio-availability has an important impact on habitability. Furthermore, the catalytic capability of copper ions has been shown to have significant importance to a major set of chemical pathways to the prebiotic synthesis of organic molecules essential to life as we know it (Sutherland, 2016; Patel et al., 2015). In this case, copper remains at low levels, but its associated mineral(s) can shed light on the conditions upon which it was liberated.

5.1.2. Improve statistics on major and trace elements

Longer dwells should also improve the statistics on targeted phases that may contain major and trace elements of interest. When one element shows an uncommonly high level of enrichment, it is important to measure not only that element more accurately but also the elements which accompany it, which can aid in the identification of the mineral involved, its origin, and geologic history. For example, phosphate minerals are often reservoirs of a wide variety of trace elements such as Ce, Sr, and Y, rare earth elements, etc. of interest for petrogenetic and fluid alteration studies (Webster and Piccoli, 2015), but with short (i.e., normal) 10-s dwells it is unlikely that we will be able to resolve these elements due to their low concentrations. Ce is particularly important to quantify as its presence, even in low concentrations, can interfere with organic detections by the SHERLOC instrument (the Raman spectrometer instrument aboard the Mars

2020 rover often deployed on the same targets as PIXL (Scheller et al., 2024 submitted). While a statistical analysis of Ce analyses by PIXL suggests Ce concentrations on the order of ~600 ppm could be resolvable with long dwells (Christian et al., 2023), recent work (VanBommel et al. 2024, submitted) considers calibration and spectral fitting uncertainties and strongly points to a threshold 1-2 orders of magnitude larger, making Ce detection by PIXL unlikely.

In addition to the phases mentioned in Section 5.1.1, PIXL's adaptive sampling rules have also been designed to trigger longer dwells on carbonate minerals in order to resolve potential trace elements. Trace element concentrations in carbonates can be used as markers of fluid interactions and fluid evolution.

In order to assess the effectiveness of the adaptive sampling rules thus far, we compiled all points identified as carbonates, spinels, and phosphates, and Mn- and Cu-enrichments in PIXL scans between sols 847 and 921 (after the implementation of the current adaptive sampling ruleset 230328). We then compared how the compositions of these phases varied by producing bulk sum spectra using short dwells only, and a combination of short and long dwells together (see Table 7 for summarized results). Bulk sum spectra are derived through the summation of energy-normalized spectra of similar characteristics (e.g., a region of interest with similar major element composition), spanning not only both detectors as well as long- and short-dwells, but also multiple individual spots within a single target scan or across multiple scans of a single target. The improved statistics offered by bulk sum spectra can provide the statistical confidence to resolve trace elements due to a better single-to-noise ratio (e.g., Christian et al. 2023).

5.2. Spinel Minerals

Spinel minerals were identified in all scans analyzed after sol 847. While these phases are ubiquitous, their small size and rarity resulted in relatively few PIXL measurements (here varying from 8 to 174 measurements/map). Due to the use of adaptive sampling however, the dwell time on these phases is dramatically increased by 39% to 263%, in comparison to integration times with normal 10 s dwells only, allowing for better detection of major and trace elements.

Bulk sum spectra for the spinel regions in each scan show that major element detections can sometimes differ when comparing normal (short) dwell sums versus short + long dwells sums (Table 7). This is especially important for estimating TiO_2 and Cr_2O_3 concentrations, which are major components in these rare minerals.

No trace elements of interest in the spinels were resolved from long dwells bulk sums, but increasing dwell time results in the removal of erroneous trace element detections in the higher energy part of the spectrum. Figure 11 shows quantified abundances of Zn and Y when considering short dwells only. An improved analysis offered through the additional statistics provided by long dwells prompted a revised concentration of a null result. In the example shown in Figure 11, whereas we might have erroneously inferred Zn and Y enrichments in spinels in the Lake Helene (sol 847) target, data from the long dwells allows us to better resolve the actual concentration of these trace elements as below detection limits.

5.3. Phosphate Minerals

Phosphate minerals were identified in 4 targets analyzed after sol 847. Similar to spinels, the small size and rarity of the phosphate minerals resulted in relatively few PIXL measurements (here varying from 2 to 270 measurements/map). When long dwells triggered by adaptive sampling are taken into account, dwell times on phosphate minerals increases by 44% to 300%.

Bulk sum spectra for the phosphate regions in each scan show that major element detections can sometimes differ when comparing normal dwell sums versus short + long dwells sums (Table 7). This is especially important for estimating P_2O_5 and CaO concentrations in these rare minerals (the main phosphate phases on Mars are the minerals apatite ($\text{Ca}_5(\text{PO}_4)_3(\text{OH},\text{F},\text{Cl})$), and merrillite ($\text{Ca}_9\text{FeMg}(\text{PO}_4)_7$) (i.e., McCubbin et al. 2016).

As was observed with the spinel analyses, increasing dwell times on the phosphate minerals resulted in the removal of erroneous quantified trace element abundances in the higher energy part of the spectrum (Table 7). No trace elements of interest (e.g., Ce, Y, or Sr) were detected.

5.4. Carbonates

There are no changes in major element concentrations or their statistical precisions when comparing long and short dwells in carbonates analyzed between sols 847 and 921. In all of the PIXL scans considered here, carbonates are abundant across the mapped area so it is understandable that the estimates from long and short dwells were similar; the long dwells did not greatly increase the cumulative integration time for carbonates with increases between 2% to 25% (Table 7).

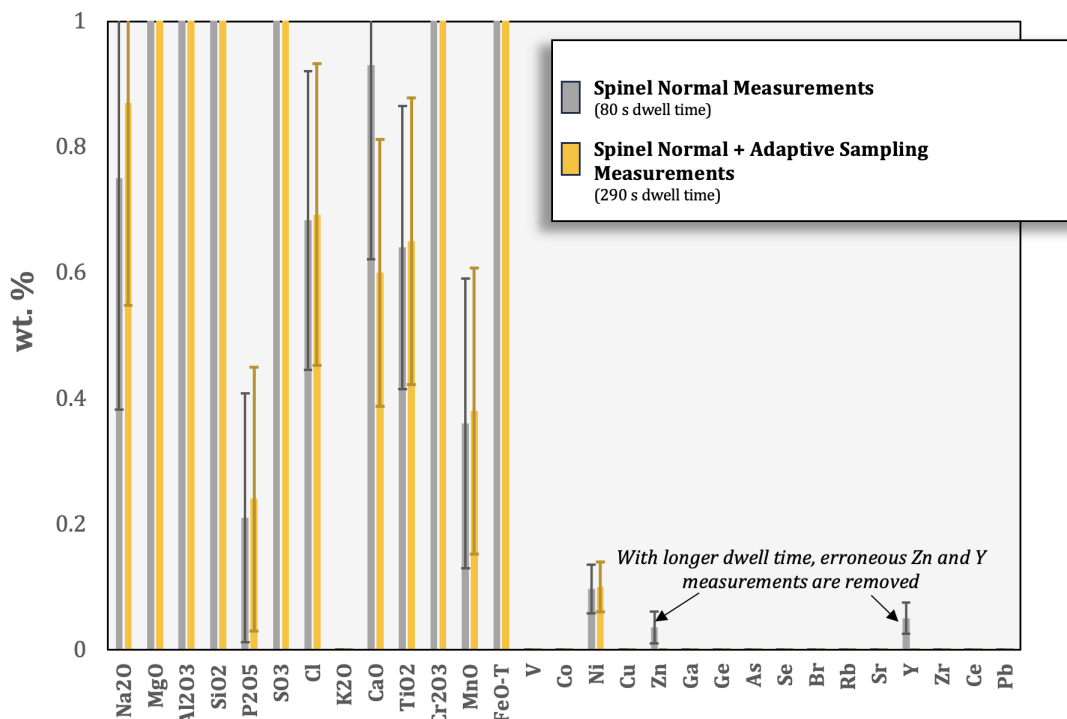


Figure 11: Elemental concentrations for spinels from the Lake Helene PIXL map (sol 847) for “normal” dwell bulk sums, and “normal” + long dwell bulk sums. Erroneous quantified abundances of trace elements Zn and Y are noted to be below detection limit with longer dwell times.

5.5. Mn- and Cu-enrichments

Adaptive sampling triggered only one long dwell associated with Mn enrichments on Sol 880, increasing the total integration time on Mn-rich phase by 23%. Here, bulk sum spectra for the Mn-rich regions shows a decrease in SiO₂ concentrations when comparing normal dwell sums versus short + long dwells sums, and no difference in trace element concentrations (Table 7).

Adaptive sampling triggered long dwells associated with Cu-enrichments on Sols 851 (10 PMCs), 874 (3 PMCs), 879 (2 PMCs), 880 (5 PMCs), and 887 (1 PMC). Careful examination of the spectra from these PMCs indicates that the majority of the long dwells were triggered by diffraction peaks (with major differences noted in the Cu peak heights between PIXL’s two detectors). True high-Cu concentrations triggered long dwells on 4 PMCs on Sol 851 resulting in a 300% increase in dwell time. When considering short dwells only, there is a quantified abundance of Zr per PIQUANT modeling, however, an improved statistical analysis provided by long dwells indicates no Zr is present above detection limits.

5.6. Discussion: Science Assessment

Based on our analysis of downlinked Mars data, we find that adaptive sampling succeeded in our goal of identifying specific high-value targets and providing better statistics on high-value compositions, thus improving assessments therein. The long dwells triggered by adaptive sampling sometimes provide better precision on major elements, but typically the values that are derived are the same, within error, as those obtained with short dwells alone. We can also often remove spurious detections of trace elements in phases of interest such as Zn, Y, Zr, and Se in spinels, phosphates, and Cu-rich regions that could affect scientific interpretations (Table 7). On the other hand, no changes in major or trace element compositions were noted for carbonates when long and short dwells were compared, likely due to the high abundance of carbonate in PIXL scans between Sols 847 and 921. As such, future adaptive sampling rulesets may be revised to reduce or remove long dwells in carbonates when in carbonate-rich lithologies.

Table 7

Summary of the dwell time increases on phases of interest targeted by adaptive sampling.

Sol	Scan	Phases of Interest	Normal Dwell Time (s)	Dwell Time with Long Dwells (s)	Dwell Time Increase	Detection Changes with Long Dwells ¹
921	Amherst Point 2	Spinel	1020	2010	97%	N/a
920	Amherst Point 1	Spinel	1740	2850	64%	N/a
880	Gabletop	Phosphates	20	80	300%	N/a
	Mountain 2	Spinel	500	1430	186%	Erroneous detection of Se removed
		Carbonates	12320	12620	2%	N/a
		Mn-rich	130	160	23%	SiO ₂ wt% refined from 22.4 ±1.1 to 26.8 ±1.33
879	Gabletop	Spinel	370	760	105%	SO ₃ wt% refined from 5.1 ±0.3 to 3.7 ±0.5
	Mountain	Carbonates	8310	9180	10%	N/a
865	Dragon's Egg	Phosphates	600	1260	110%	P ₂ O ₅ wt% refined from 10.4 ±0.5 to 7.9 ±0.4
	Rock 2					CaO wt% refined from 10.6 ±0.5 to 8.9 ±0.4
						Al ₂ O ₃ wt% refined from 10.4 ±0.5 to 11.9 ±0.6
						Erroneous detection of Zr removed
		Spinel	500	1010	102%	SO ₃ wt% refined from 2.4 ±0.5 to 3.5 ±0.5
860	Dragon's Egg	Phosphates	2700	3900	44%	CaO wt% refined from 17.7 ±0.9 to 14.4 ±0.7
	Rock					SO ₃ wt% refined from 21.9 ±1.2 to 15.9 ±0.8
						Al ₂ O ₃ wt% refined from 5.78 ±0.3 to 7.87 ±0.4
						MgO wt% refined from 10.5 ±0.5 to 12 ±0.6
						SiO ₂ wt% refined from 21.8 ±1.1 to 27.1 ±1.4
		Spinel	310	430	39%	SO ₃ wt% refined from 14.1 ±0.87 to 10.4 ±0.5
						CaO wt% refined from 10.1 ±0.5 to 8.1 ±0.4
						TiO ₂ wt% refined from 5.1 ±0.3 to 6.3 ±0.3
852	Lake Haiyaha 2	Phosphates	20	80	300%	Erroneous detection of Zr removed
		Spinel	460	1390	202%	Cr ₂ O ₃ wt% refined from 8.3 ±0.4 to 7.3 ±0.4
		Carbonates	1310	1640	25%	N/a
851	Lake Haiyaha 1	Spinel	90	270	200%	Erroneous detection of Zn removed
		Cu-rich	40	160	300%	Erroneous detection of Zr removed
847	Lake Helene	Spinel	80	290	263%	Erroneous detections of Zn and Y removed

¹ Detection changes are defined as element concentrations differing outside of error.

The results presented in this paper suggest that detection thresholds interpreted from short dwells might be too low for some elements and that adaptive sampling provides more realistic limits. Adaptive sampling has also been shown to provide improved data on rare phases which would otherwise be difficult because of their small size and scarcity, with little effect on PIXL operations time and power constraints. As noted in the preceding sections, the typical adaptive sampling budget of 45 points on a 5 x 7 mm PIXL scan results in 22.5 minutes of extra scan time. If the 22.5 minutes were instead used for standard 10-s dwells, the area of a typical PIXL scan (2337 total analysis points) would increase by only ~6% (22.5 minutes = 135 additional 10-s dwells). As summarized in this section and Table 7, this small operational trade-off results in increases in dwell times on phases of interest by up to 300%, and increases our confidence in the interpretation of trace element detections.

6. Conclusion

We have successfully demonstrated new adaptive sampling technology with PIXL on the Mars *Perseverance* rover. To our knowledge, this has enabled the first autonomous decision-making based on real-time compositional analysis by an exploration spacecraft. Almost all the rules were implemented through machine learning, trained with compositional analysis of PIXL Mars data taken earlier in the mission. These rules are simple Linear Classifiers that use pseudo-intensities, approximations of the intensities of spectral peaks, to determine the presence or absence of compositions of interest. The rules were shown to work particularly well for spinel minerals (identified by enrichments in Cr₂O₃ and TiO₂) and phosphate minerals (identified by enrichments in P₂O₅) where they increased the dwell times by up to 300% and aided in the interpretation of detections of trace elements. Although the carbonate rule had a 12% true positive rate and did not significantly enhance the interpretation of data, it is nonetheless remarkable that it worked as well as it did, because PIXL does not directly observe the characteristic fluorescence X-rays from C. The new Zr rule, despite never being given an opportunity to trigger, was also shown in simulations to work correctly and will further enhance the science return of the Mars *Perseverance* rover in its continuing explorations.

Acknowledgments

The work described in this paper was partially carried out at the Jet Propulsion Laboratory, California Institute of Technology, under a contract with the National Aeronautics and Space Administration. We are grateful to Mars 2020 team members who participated in tactical and strategic science operations. We thank the support from NASA for the Phase E funding. Particular thanks to Morgan Cable, Joel Hurowitz, and the PIXL Science Team. We thank the following for help during laboratory development and Integration & Test: Mitch Au, Hank Conley, Marc Foote, Christina Hernandez, Christopher Hummel, Joan Ervin, Ami Kitiyakari, Raúl Romero, Rogelio Rosas, Michael Sondheim, Eugenie Song, and Michael Umana. We are also grateful for ongoing surface operations coordinated by Jason Van Beek, Adrian Galvin, James Gerhard, and Nicholas Tallarida. We are grateful for support of the PIXL data pipeline and the PIXLISE team; in particular Scott Davidoff, Peter Nemere, and Kyle Uckert. PRL is grateful to Felix Lawson for guidance during the early stages of software development of machine learning.

PRL, LAW, RWD, and CMH are supported by Mars 2020 Phase E funding, DRT, MSG, and BJB were supported by Mars 2020 Phase C funding, TVK is supported by a Canadian Space Agency M2020 Participating Scientist grant. SJV was supported by M2020 PS Grant #80NSSC21K0328.

Declaration of competing interest

The authors declare that they have no known competing financial interests or personal relationships that could have appeared to influence the work reported in this paper.

Data availability

The analysis presented here is based on Localized Full Spectra (RFS), which are publicly available in the *PIXL Processed data collection* at the Geosciences Node of the Planetary Data System (PDS; doi 10.17189/1522645; <https://pds-geosciences.wustl.edu/missions/mars2020/pixl.htm>).

CRedit authorship contribution statement

Peter R. Lawson: Conceptualization, Methodology, Software, Validation, Formal analysis, Investigation, Writing - Original Draft, Writing - Review & Editing. **Tanya V. Kizovski:** Methodology, Validation, Formal analysis, Writing - Original Draft, Writing - Review & Editing. **Michael M. Tice:** Conceptualization, Methodology, Validation, Formal analysis, Writing - Review & Editing. **Benton C. Clark III:** Conceptualization, Validation, Formal analysis, Writing - Review & Editing. **Scott J. VanBommel:** Formal analysis, Writing - Review & Editing. **David R. Thompson:** Conceptualization, Methodology, Software, Writing - Original Draft. **Lawrence A. Wade:** Conceptualization, Methodology. **Robert W. Denise:** Software. **Christopher M. Heirwegh:** Software, Data Curation, Writing - Review & Editing. **W. Timothy Elam:** Methodology, Software, Data Curation. **Mariek E. Schmidt:** Formal analysis, Writing - Review & Editing. **Yang Liu:** Conceptualization, Methodology, Writing - Review & Editing. **Abigail C. Allwood:** Conceptualization, Funding acquisition. **Martin S. Gilbert:** Software. **Benjamin J. Bornstein:** Software.

A. Supplementary data

Supplementary data to this article can be found online at TBD.

References

- Allwood, A.C., Wade, L.A., Foote, M.C., Elam, W.T., Hurowitz, J.A., Battel, S., Dawson, D.E., Denise, R.W., Ek, E.M., Gilbert, M.S., King, M.E., Liebe, C.C., Parker, T., Pedersen, D.A.K., Randall, D.P., Sharrow, R.F., Sondheim, M.E., Allen, G., Arnett, K., Au, M.H., Basset, C., Benn, M., Bousman, J.C., Braun, D., Calvet, R.J., Clark, B., Cinquini, L., Conaby, S., Conley, H.A., Davidoff, S., Delaney, J., Denver, T., Diaz, E., Doran, G.B., Ervin, J., Evans, M., Flannery, D.O., Gao, N., Gross, J., Grotzinger, J., Hannah, B., Harris, J.T., Harris, C.M., He, Y., Heirwegh, C.M., Hernandez, C., Hertzberg, E., Hodyss, R.P., Holden, J.R., Hummel, C., Jadusingh, M.A., Jørgensen, J.L., Kawamura, J.H., Kitiyakara, A., Kozaczek, K., Lambert, J.L., Lawson, P.R., Liu, Y., Luchik, T.S., Macneal, K.M., Madsen, S.N., McLennan, S.M., McNally, P., Meras, P.L., Muller, R.E., Napoli, J., Naylor, B.J., Nemere, P., Ponomarev, I., Perez, R.M., Pootrakul, N., Romero, R.A., Rosas, R., Sachs, J., Schaefer, R.T., Schein, M.E., Setterfield, T.P., Singh, V., Song, E., Soria, M.M., Stek, P.C., Tallarida, N.R., Thompson, D.R., Tice, M.M., Timmermann, L., Torossian, V., Treiman, A., Tsai, S., Uckert, K., Villalvazo, J., Wang, M., Wilson, D.W., Worel, S.C., Zamani, P., Zappe,

- M., Zhong, F., Zimmerman, R., 2020. PIXL: Planetary Instrument for X-Ray Lithochemistry. *Space Science Reviews* 216, 1–132. URL: <https://doi.org/10.1007/s11214-020-00767-7>.
- Arvidson, R.E., Squyres, S.W., Morris, R.V., Knoll, A.H., Gellert, R., Clark, B.C., Catalano, J.G., Jolliff, B.L., McLennan, S.M., Herkenhoff, K.E., VanBommel, S., Mittlefehldt, D.W., Grotzinger, J.P., Guinness, E.A., Johnson, J.R., Bell, J.F., Farrand, W.H., Stein, N., Fox, V.K., Golombek, M.P., Hinkle, M.A., Calvin, W.M., Souza, P.A.D., 2016. High concentrations of manganese and sulfur in deposits on Murray ridge, Endeavour crater, Mars. *American Mineralogist* 101, 1389–1405. URL: <https://doi.org/10.2138/am-2016-5599>, doi:doi:10.2138/am-2016-5599.
- Berger, J., King, P., Gellert, R., Clark, B., O’Connell-Cooper, C., Thompson, L., Van Bommel, S., A.S., Y., 2019. Manganese enrichment pathways relevant to Gale crater, Mars: Evaporative concentration and chlorine-induced precipitation, in: *Lunar and Planetary Science Conference, The Woodlands (Texas), United States*. URL: <https://hal.science/hal-04446048>.
- Berger, J.A., King, P.L., Gellert, R., Clark, B.C., Flood, V.A., McCraig, M.A., Ming, D.W., O’Connell-Cooper, C.D., Schmidt, M.E., Thompson, L.M., VanBommel, S.J.V., Wilhelm, B., Yen, A.S., 2022. Manganese mobility in Gale crater, Mars: Leached bedrock and localized enrichments. *Journal of Geophysical Research: Planets* 127, e2021JE007171. URL: <https://agupubs.onlinelibrary.wiley.com/doi/abs/10.1029/2021JE007171>, doi:<https://doi.org/10.1029/2021JE007171>, arXiv:<https://agupubs.onlinelibrary.wiley.com/doi/pdf/10.1029/2021JE007171>, e2021JE007171 2021JE007171.
- Candela, A., Thompson, D., Dobrea, E.N., Wettergreen, D., 2017. Planetary robotic exploration driven by science hypotheses for geologic mapping, in: *2017 IEEE/RSJ International Conference on Intelligent Robots and Systems (IROS)*, IEEE. pp. 3811–3818. doi:10.1109/IROS.2017.8206231.
- Castano, A., Fukunaga, A., Biesiadecki, J., Neakrase, L., Whelley, P., Greeley, R., Lemmon, M., Castano, R., Chien, S., 2008. Automatic detection of dust devils and clouds on Mars. *Machine Vision and Applications* 19, 467–482. URL: <https://doi.org/10.1007/s00138-007-0081-3>.
- Christian, J.R., VanBommel, S.J., Elam, W.T., Ganly, B., Hurowitz, J.A., Heirwegh, C.M., Allwood, A.C., Clark, B.C., Kizovski, T.V., Knight, A.L., 2023. Statistical characterization of pixl trace element detection limits. *Acta Astronautica* 212, 534–540. URL: <https://www.sciencedirect.com/science/article/pii/S0094576523004393>, doi:<https://doi.org/10.1016/j.actaastro.2023.08.032>.
- De Vos, W., Gregorauskiene, V., Marsina, K., Salminen, R., Salpeteur, I., Tarvainen, T., O’Connor, P., Demetriades, A., Pirc, S., Batista, M., Bidovec, M., Bel-lan, A., Birke, M., Breward, N., De Vivo, B., Duris, M., Halamic, J., Klein, P., Lima, A., Locutura, J., Lis, J., Mazreku, A., Ottesen, R., Pasieczna, A., Petersell, V., Reeder, S., Siewers, U., Slaninka, I., 2006. Distribution of elements in subsoil and topsoil. pp. 21–29. URL: <http://weppi.gtk.fi/publ/foregsatlas/article2.php?id=21>.
- Estlin, T.A., Bornstein, B.J., Gaines, D.M., Anderson, R.C., Thompson, D.R., Burl, M., Castano, R., Judd, M., 2012. AEGIS automated science targeting for the MER Opportunity rover. *ACM Transactions on Intelligent Systems and Technology (TIST)* 3, 1–19. URL: <https://doi.org/10.1145/2168752.2168764>, doi:10.1145/2168752.2168764.
- Farley, K.A., Stack, K.M., Shuster, D.L., Horgan, B.H.N., Hurowitz, J.A., Tarnas, J.D., Simon, J.I., Sun, V.Z., Scheller, E.L., Moore, K.R., McLennan, S.M., Vasconcelos, P.M., Wiens, R.C., Treiman, A.H., Mayhew, L.E., Beyssac, O., Kizovski, T.V., Tosca, N.J., Williford, K.H., Crumpler, L.S., Beegle, L.W., Bell, J.F., Ehlmann, B.L., Liu, Y., Maki, J.N., Schmidt, M.E., Allwood, A.C., Amundsen, H.E.F., Bhartia, R., Bosak, T., Brown, A.J., Clark, B.C., Cousin, A., Forni, O., Gabriel, T.S.J., Goreva, Y., Gupta, S., Hamran, S.E., Herd, C.D.K., Hickman-Lewis, K., Johnson, J.R., Kah, L.C., Kelemen, P.B., Kinch, K.B., Mandon, L., Mangold, N., Quantin-Nataf, C., Rice, M.S., Russell, P.S., Sharma, S., Siljeström, S., Steele, A., Sullivan, R., Wadhwa, M., Weiss, B.P., Williams, A.J., Wogsland, B.V., Willis, P.A., Acosta-Maeda, T.A., Beck, P., Benzerara, K., Bernard, S., Burton, A.S., Cardarelli, E.L., Chide, B., Clavé, E., Cloutis, E.A., Cohen, B.A., Czaja, A.D., Debaille, V., Dehouck, E., Fairén, A.G., Flannery, D.T., Fleron, S.Z., Fouchet, T., Frydenvang, J., Garczynski, B.J., Gibbons, E.F., Hausrath, E.M., Hayes, A.G., Henneke, J., Jørgensen, J.L., Kelly, E.M., Lasue, J., Mouélic, S.L., Madariaga, J.M., Maurice, S., Merusi, M., Meslin, P.Y., Milkovich, S.M., Million, C.C., Moeller, R.C., Núñez, J.I., Ollila, A.M., Paar, G., Paige, D.A., Pedersen, D.A.K., Pilleri, P., Pilorget, C., Pinet, P.C., Rice, J.W., Royer, C., Sautter, V., Schulte, M., Sephton, M.A., Sharma, S.K., Sholes, S.F., Spanovich, N., Clair, M.S., Tate, C.D., Uckert, K., VanBommel, S.J., Yanchilina, A.G., Zorzano, M.P., 2022. Aqueously altered igneous rocks sampled on the floor of jezero crater, mars. *Science* 377, eabo2196. URL: <https://www.science.org/doi/abs/10.1126/science.abo2196>, doi:10.1126/science.abo2196, arXiv:<https://www.science.org/doi/pdf/10.1126/science.abo2196>.
- Farley, K.A., Williford, K.H., Stack, K.M., Bhartia, R., Chen, A., de la Torre, M., Hand, K., Goreva, Y., Herd, C.D., Hueso, R., et al., 2020. Mars 2020 mission overview. *Space Science Reviews* 216, 1–41. URL: <https://doi.org/10.1007/s11214-020-00762-y>.
- Forni, O., Bedford, C.C., Royer, C., Liu, Y., Wiens, R.C., Dehouck, E., Meslin, P.Y., Udry, A., Beyssac, O., Gabriel, T.S., Beck, P., Gasnault, O., Quantin-Nataf, C., Johnson, J.R., Schröder, S., Pilleri, P., Debaille, V., Manelsy, H.T., Clark, B.C., Cousin, A., Maurice, S., Clegg, S.M., 2024. Nickel-copper deposits on Mars? discovery of ore-grade abundances, and implications on formation and alteration, in: *Lunar and Planetary Science Conference, The Woodlands (Texas), United States*. URL: <https://hal.science/hal-04446048>.
- Francis, R., Estlin, T., Doran, G., Johnstone, S., Gaines, D., Verma, V., Burl, M., Frydenvang, J., Montaño, S., Wiens, R., et al., 2017. AEGIS autonomous targeting for ChemCam on Mars Science Laboratory: Deployment and results of initial science team use. *Science Robotics* 2, eaan4582. URL: <https://www.science.org/doi/abs/10.1126/scirobotics.aan4582>.
- Goetz, W., Dehouck, E., Gasda, P.J., Johnson, J.R., Meslin, P.Y., Lanza, N.L., Wiens, R.C., Rapin, W., Frydenvang, J., Payré, V., Gasnault, O., 2023. Detection of copper by the ChemCam instrument along Curiosity’s traverse in Gale crater, Mars: Elevated abundances in Glen Torridon. *Journal of Geophysical Research: Planets* 128, e2021JE007101. URL: <https://agupubs.onlinelibrary.wiley.com/doi/abs/10.1029/2021JE007101>, doi:<https://doi.org/10.1029/2021JE007101>, arXiv:<https://agupubs.onlinelibrary.wiley.com/doi/pdf/10.1029/2021JE007101>, e2021JE007101 2021JE007101.
- Goodrich, C.A., Herd, C.D.K., Taylor, L.A., 2003. Spinel and oxygen fugacity in olivine-phyric and ilherzolitite shergottites. *Meteoritics & Planetary Science* 38, 1773–1792. URL: <https://onlinelibrary.wiley.com/doi/abs/10.1111/j.1945-5100.2003.tb00014.x>, doi:<https://doi.org/10.1111/j.1945-5100.2003.tb00014.x>, arXiv:<https://onlinelibrary.wiley.com/doi/pdf/10.1111/j.1945-5100.2003.tb00014.x>.

- Heirweh, C.M., Elam, W.T., Liu, Y., Das, A., Hummel, C., Naylor, B., Wade, L.A., Allwood, A.C., Hurowitz, J.A., Armstrong, L.G., Bacop, N., O'Neil, L.P., Sinclair, K.P., Sondheim, M.E., Denise, R.W., Lawson, P.R., Rosas, R., Kawamura, J.H., Au, M.H., Kitiyakara, A., Foote, M.C., Romero, R.A., Anderson, M.S., Rossman, G.R., au2, B.C.C.I., 2024. Pre-flight calibration of PIXL for X-ray fluorescence elemental quantification. URL: <https://arxiv.org/abs/2402.01544>, arXiv:2402.01544.
- Heirweh, C.M., Elam, W.T., O'Neil, L.P., Sinclair, K.P., Das, A., 2022. The focused beam X-ray fluorescence elemental quantification software package PIQUANT. *Spectrochim. Acta B* 196, 106520. URL: <https://doi.org/10.1016/j.sab.2022.106520>.
- Herd, C.D.K., Moser, D.E., Tait, K., Darling, J.R., Shaulis, B.J., McCoy, T.J., 2018. Crystallization of Baddeleyite in Basaltic Rocks from Mars, and Comparisons with the Earth, Moon, and Vesta. *American Geophysical Union (AGU) chapter 6*. pp. 137–166. URL: <https://agupubs.onlinelibrary.wiley.com/doi/abs/10.1002/9781119227250.ch6>, doi:<https://doi.org/10.1002/9781119227250.ch6>, arXiv:<https://agupubs.onlinelibrary.wiley.com/doi/pdf/10.1002/9781119227250.ch6>.
- Lanza, N., Wiens, R., Arvidson, R., Clark, B., Fischer, W., Gellert, R., Grotzinger, J., Hurowitz, J., McLennan, S., Morris, R., Rice, M., Bell, J., Berger, J., Blaney, D., Blank, J., Bridges, N., Calef, F., Campbell, J., Clegg, S., Cousin, A., Edgett, K., Fabre, C., Fisk, M., Forni, O., Frydenvang, J., Hardy, K., Hardgrove, C., Johnson, J., Kah, L., Lasue, J., Le Mouélic, S., Malin, M., Mangold, N., Martin-Torres, J., Maurice, S., McBride, M., Ming, D., Newsom, H., Schroder, S., Thompson, L., Treiman, A., VanBommel, S., Vaniman, D., Zorzano, M., 2015. Oxidation of manganese at Kimberley, Gale crater: More free oxygen in Mars' past? URL: <https://www.hou.usra.edu/meetings/lpsc2015/>. IPI Contribution No. 1832, p.2893; 46th Lunar and Planetary Science Conference ; Conference date: 16-03-2015 Through 20-03-2015.
- Lanza, N.L., Fischer, W.W., Wiens, R.C., Grotzinger, J., Ollila, A.M., Cousin, A., Anderson, R.B., Clark, B.C., Gellert, R., Mangold, N., Maurice, S., Le Mouélic, S., Nachon, M., Schmidt, M., Berger, J., Clegg, S.M., Forni, O., Hardgrove, C., Melikechi, N., Newsom, H.E., Sautter, V., 2014. High manganese concentrations in rocks at Gale crater, Mars. *Geophysical Research Letters* 41, 5755–5763. URL: <https://agupubs.onlinelibrary.wiley.com/doi/abs/10.1002/2014GL060329>, doi:<https://doi.org/10.1002/2014GL060329>, arXiv:<https://agupubs.onlinelibrary.wiley.com/doi/pdf/10.1002/2014GL060329>.
- Liu, Y., Tice, M.M., Schmidt, M.E., Treiman, A.H., Kizovski, T.V., Hurowitz, J.A., Allwood, A.C., Henneke, J., Pedersen, D.A.K., VanBommel, S.J., Jones, M.W.M., Knight, A.L., Orenstein, B.J., Clark, B.C., Elam, W.T., Heirweh, C.M., Barber, T., Beegle, L.W., Benzerara, K., Bernard, S., Beyssac, O., Bosak, T., Brown, A.J., Cardarelli, E.L., Catling, D.C., Christian, J.R., Cloutis, E.A., Cohen, B.A., Davidoff, S., Fairén, A.G., Farley, K.A., Flannery, D.T., Galvin, A., Grotzinger, J.P., Gupta, S., Hall, J., Herd, C.D.K., Hickman-Lewis, K., Hodyss, R.P., Horgan, B.H.N., Johnson, J.R., Jørgensen, J.L., Kah, L.C., Maki, J.N., Mandon, L., Mangold, N., McCubbin, F.M., McLennan, S.M., Moore, K., Nachon, M., Nemere, P., Notherdurft, L.D., Núñez, J.I., O'Neil, L., Quantin-Nataf, C.M., Sautter, V., Shuster, D.L., Siebach, K.L., Simon, J.I., Sinclair, K.P., Stack, K.M., Steele, A., Tarnas, J.D., Tosca, N.J., Uckert, K., Udry, A., Wade, L.A., Weiss, B.P., Wiens, R.C., Williford, K.H., Zorzano, M.P., 2022. An olivine cumulate outcrop on the floor of jezero crater, mars. *Science* 377, 1513–1519. URL: <https://www.science.org/doi/abs/10.1126/science.abo2756>, doi:10.1126/science.abo2756, arXiv:<https://www.science.org/doi/pdf/10.1126/science.abo2756>.
- McCubbin, F.M., Boyce, J.W., Srinivasan, P., Santos, A.R., Elardo, S.M., Filiberto, J., Steele, A., Shearer, C.K., 2016. Heterogeneous distribution of H₂O in the martian interior: Implications for the abundance of H₂O in depleted and enriched mantle sources. *Meteoritics & Planetary Science* 51, 2036–2060. URL: <https://onlinelibrary.wiley.com/doi/abs/10.1111/maps.12639>, doi:<https://doi.org/10.1111/maps.12639>, arXiv:<https://onlinelibrary.wiley.com/doi/pdf/10.1111/maps.12639>.
- Moeller, R., Jandura, L., Rosette, K., Robinson, M., Samuels, J., Silverman, M., Brown, K., Duffy, E., Yazzie, A., Jens, E., Brockie, I., White, L., Goreva, Y., Zorn, T., Okon, A., Lin, J., Frost, M., Collins, C., Williams, J., et al., 2021. The sampling and caching subsystem (SCS) for the scientific exploration of Jezero crater by the Mars 2020 Perseverance rover. *Space Sci. Rev.* 217. URL: <https://doi.org/10.1007/s11214-020-00783-7>.
- Nemere, P., Barber, T., Stonebraker, R., Fedell, S.M., Galvin, A., Davidoff, S., 2024. PIXLISE core. Zenodo URL: <https://doi.org/10.5281/zenodo.10183256>.
- Papike, J., Karner, J., Shearer, C., Burger, P., 2009. Silicate mineralogy of martian meteorites. *Geochimica et Cosmochimica Acta* 73, 7443–7485. URL: <https://www.sciencedirect.com/science/article/pii/S0016703709005651>, doi:<https://doi.org/10.1016/j.gca.2009.09.008>.
- Patel, B.H., Percivalle, C., Ritson, D.J., Duffy, C.D., Sutherland, J.D., 2015. Common origins of RNA, protein and lipid precursors in a cyanosulfidic protometabolism. *Nature Chemistry* 7, 301–307. doi:<https://doi.org/10.1038/nchem.2202>.
- Payré, V., Fabre, C., Sautter, V., Cousin, A., Mangold, N., Deit, L.L., Forni, O., Goetz, W., Wiens, R.C., Gasnault, O., Meslin, P.Y., Lasue, J., Rapin, W., Clark, B., Nachon, M., Lanza, N.L., Maurice, S., 2019. Copper enrichments in the Kimberley formation in Gale crater, Mars: Evidence for a Cu deposit at the source. *Icarus* 321, 736–751. URL: <https://www.sciencedirect.com/science/article/pii/S0019103518304779>, doi:<https://doi.org/10.1016/j.icarus.2018.12.015>.
- Pedregosa, F., Varoquaux, G., Gramfort, A., Michel, V., Thirion, B., Blondel, M., Prettenhofer, P., Weiss, R., Dubourg, V., Vanderplas, J., Passos, A., Cournapeau, D., Brucher, M., Perrot, M., Édouard Duchesnay, 2011. Scikit-learn: Machine learning in python. *Journal of Machine Learning Research* 12, 2825–2830. URL: <http://jmlr.org/papers/v12/pedregosa11a.html>.
- Russell, S.J., Norvig, P., 2020. *Artificial Intelligence: A Modern Approach* (4th Edition). Pearson. URL: <http://aima.cs.berkeley.edu/>.
- Scheller, E., Bosak, T., McCubbin, F., Williford, K., Siljeström, S., Jakubek, R., Eckley, S., Morris, R., Bykov, S., Kizovski, T., Asher, S., Berger, E., Bower, D., Cardarelli, E., Ehlmann, B., Fornaro, T., Fox, A., Haney, N., Hand, K., Roppel, R., Sharma, S., Steele, A., Uckert, K., Yanchilina, A., Beyssac, O., Farley, K., Henneke, J., Heirweh, C., Pedersen, D., Liu, Y., Schmidt, M., Sephton, M., Shuster, D., Weiss, B., 2024 submitted. Inorganic interpretation of luminescent materials encountered by the Perseverance rover on Mars. *Science Advances*.
- Sun, V.Z., Hand, K.P., Stack, K.M., Farley, K.A., Simon, J.I., Newman, C., Sharma, S., Liu, Y., Wiens, R.C., Williams, A.J., Tosca, N., Alwmark, S., Beyssac, O., Brown, A., Calef, F., Cardarelli, E.L., Clavé, E., Cohen, B., Corpolongo, A., Czaja, A.D., Del Sesto, T., Fairén, A., Fornaro, T., Fouchet, T., Garczynski, B., Gupta, S., Herd, C.D.K., Hickman-Lewis, K., Horgan, B., Johnson, J., Kinch, K., Kizovski, T., Kronyak, R., Lange, R., Mandon, L., Milkovich, S., Moeller, R., Núñez, J., Paar, G., Pyrzak, G., Quantin-Nataf, C., Shuster, D.L., Siljeström, S., Steele, A., Tice, M., Toupet, O., Udry, A., Vaughan, A., Wogsland, B., 2023. Overview and results from the Mars 2020 Perseverance rover's first science campaign on the Jezero crater floor. *Journal of Geophysical Research: Planets* 128,

- e2022JE007613. URL: <https://agupubs.onlinelibrary.wiley.com/doi/abs/10.1029/2022JE007613>, doi:<https://doi.org/10.1029/2022JE007613>, arXiv:<https://agupubs.onlinelibrary.wiley.com/doi/pdf/10.1029/2022JE007613>. e2022JE007613 2022JE007613.
- Sutherland, J.D., 2016. The origin of life—out of the blue. *Angewandte Chemie International Edition* 55, 104–121. URL: <https://onlinelibrary.wiley.com/doi/abs/10.1002/anie.201506585>, doi:<https://doi.org/10.1002/anie.201506585>, arXiv:<https://onlinelibrary.wiley.com/doi/pdf/10.1002/anie.201506585>.
- Thompson, D.R., Flannery, D.T., Kiran, R.A., Allwood, A.C., Bue, B.D., Clark, B., Elam, W.T., Estlin, T., Hodyss, R., Hurowitz, J.A., Liu, Y., Wade, L., 2015. Automating X-ray fluorescence analysis for rapid astrobiology surveys. *Astrobiology* 15, 961–976. URL: <https://doi.org/10.1089/ast.2015.1349>, doi:<https://doi.org/10.1089/ast.2015.1349>.
- Thompson, D.R., Wettergreen, D.S., Peralta, F.J.C., 2011. Autonomous science during large-scale robotic survey. *Journal of Field Robotics* 28, 542–564.
- Tice, M.M., Hurowitz, J.A., Allwood, A.C., Jones, M.W.M., Orenstein, B.J., Davidoff, S., Wright, A.P., Pedersen, D.A., Henneke, J., Tosca, N.J., Moore, K.R., Clark, B.C., McLennan, S.M., Flannery, D.T., Steele, A., Brown, A.J., Zorzano, M.P., Hickman-Lewis, K., Liu, Y., VanBommel, S.J., Schmidt, M.E., Kizovski, T.V., Treiman, A.H., O’Neil, L., Fairén, A.G., Shuster, D.L., Gupta, S., Team, T.P., 2022. Alteration history of séítah formation rocks inferred by pixl x-ray fluorescence, x-ray diffraction, and multispectral imaging on mars. *Science Advances* 8, eabp9084. URL: <https://www.science.org/doi/abs/10.1126/sciadv.abp9084>, doi:[10.1126/sciadv.abp9084](https://doi.org/10.1126/sciadv.abp9084), arXiv:<https://www.science.org/doi/pdf/10.1126/sciadv.abp9084>.
- Treiman, A.H., Lanza, N.L., VanBommel, S., Berger, J., Wiens, R., Bristow, T., Johnson, J., Rice, M., Hart, R., McAdam, A., Gasda, P., Meslin, P.Y., Yen, A., Williams, A.J., Vasavada, A., Vaniman, D., Tu, V., Thorpe, M., Swanner, E.D., Seeger, C., Schwenzer, S.P., Schröder, S., Rampe, E., Rapin, W., Ralston, S.J., Peretyazhko, T., Newsom, H., Morris, R.V., Ming, D., Loche, M., Le Mouélic, S., House, C., Hazen, R., Grotzinger, J.P., Gellert, R., Gasnault, O., Fischer, W.W., Essunfeld, A., Downs, R.T., Downs, G.W., Dehouck, E., Crossey, L.J., Cousin, A., Comellas, J.M., Clark, J.V., Clark, B., Chipera, S., Caravaca, G., Bridges, J., Blake, D.F., Anderson, R., 2023. Manganese-iron phosphate nodules at the Groken site, Gale crater, Mars. *Minerals* 13. URL: <https://www.mdpi.com/2075-163X/13/9/1122>, doi:[10.3390/min13091122](https://doi.org/10.3390/min13091122).
- Udry, A., Howarth, G.H., Herd, C.D.K., Day, J.M.D., Lapen, T.J., Filiberto, J., 2020. What martian meteorites reveal about the interior and surface of Mars. *Journal of Geophysical Research: Planets* 125, e2020JE006523. URL: <https://agupubs.onlinelibrary.wiley.com/doi/abs/10.1029/2020JE006523>, doi:<https://doi.org/10.1029/2020JE006523>, arXiv:<https://agupubs.onlinelibrary.wiley.com/doi/pdf/10.1029/2020JE006523>. e2020JE006523 2020JE006523.
- Van Grieken, R., Markowicz, A., 2001. *Handbook of X-Ray Spectrometry*. CRC Press, New York.
- VanBommel, S., Berger, J., Gellert, R., O’Connell-Cooper, C., McCraig, M., Thompson, L., Fedo, C., Des Marais, D., Fey, D., Yen, A., Clark, B., Treiman, A., Boyd, N., 2023. Elemental composition of manganese- and phosphorus-rich nodules in the Knockfarril Hill member, Gale crater, Mars. *Icarus* 392, 115372. URL: <https://www.sciencedirect.com/science/article/pii/S001910352200464X>, doi:<https://doi.org/10.1016/j.icarus.2022.115372>.
- VanBommel, S., Gellert, R., Berger, J., McCraig, M., O’Connell-Cooper, C., Thompson, L., Yen, A., Boyd, N., Lanza, N., Ollila, A., 2022. Constraining the chemical depth profile of a manganese-rich surface layer in Gale crater, Mars. *Spectrochimica Acta Part B: Atomic Spectroscopy* 191, 106410. URL: <https://www.sciencedirect.com/science/article/pii/S0584854722000544>, doi:<https://doi.org/10.1016/j.sab.2022.106410>.
- VanBommel, S., Gellert, R., Berger, J., Yen, A., Boyd, N., 2019a. Mars Science Laboratory alpha particle X-ray spectrometer trace elements: Situational sensitivity to Co, Ni, Cu, Zn, Ga, Ge, and Br. *Acta Astronautica* 165, 32–42. URL: <https://www.sciencedirect.com/science/article/pii/S0094576519312445>, doi:<https://doi.org/10.1016/j.actaastro.2019.08.026>.
- VanBommel, S., Gellert, R., Boyd, N., Hanania, J., 2019b. Empirical simulations for further characterization of the Mars Science Laboratory alpha particle X-ray spectrometer: An introduction to the ACES program. *Nuclear Instruments and Methods in Physics Research Section B: Beam Interactions with Materials and Atoms* 441, 79–87. URL: <https://www.sciencedirect.com/science/article/pii/S0168583X18307626>, doi:<https://doi.org/10.1016/j.nimb.2018.12.040>.
- VanBommel, S.J., Sharma, S., Kizovski, T.V., Heirwegh, C.M., Christian, J.R., Knight, A.L., Ganly, B., Allwood, A.C., Hurowitz, J.A., Tice, M.M., Cable, M.L., Elam, W.T., Jones, M.W.M., Clark, B.C., Schmidt, M.E., Liu, Y., Das, A., 2024. Constraining the cerium content of rocks and regolith in Jezero crater, Mars. Manuscript submitted for publication.
- Verma, V., Maimone, M.W., Gaines, D.M., Francis, R., Estlin, T.A., Kuhn, S.R., Rabideau, G.R., Chien, S.A., McHenry, M.M., Graser, E.J., Rankin, A.L., Thiel, E.R., 2023. Autonomous robotics is driving Perseverance rover’s progress on Mars. *Science Robotics* 8, eadi3099. URL: <https://www.science.org/doi/abs/10.1126/scirobotics.adi3099>, doi:[10.1126/scirobotics.adi3099](https://doi.org/10.1126/scirobotics.adi3099), arXiv:<https://www.science.org/doi/pdf/10.1126/scirobotics.adi3099>.
- Webster, J.D., Piccoli, P.M., 2015. Magmatic Apatite: A Powerful, Yet Deceptive, Mineral. *Elements* 11, 177–182. URL: <https://doi.org/10.2113/gselements.11.3.177>, doi:[10.2113/gselements.11.3.177](https://doi.org/10.2113/gselements.11.3.177), arXiv:https://pubs.geoscienceworld.org/msa/elements/article-pdf/11/3/177/3110886/177_ELEM_v11n3.pdf.
- Wettergreen, D., Foil, G., Furlong, M., Thompson, D.R., 2014. Science autonomy for rover subsurface exploration of the Atacama desert. *AI Magazine* 35, 47–60.